JGR Earth Surface

RESEARCH ARTICLE
10.1029/2025JF008354

Linking Dynamic Parameters and Seismic Signals of Granular Flows in Different Flow Regimes: An Experimental Assessment of Effects of Particle Composition

Xinzhi Zhou[1], Yifei Cui[1], Zhen Zhang[2], Lingling Ye[3], and Jun Fang[4]

[1]State Key Laboratory of Hydroscience and Engineering, Tsinghua University, Beijing, China, [2]Swiss Federal Institute for Forest, Snow and Landscape Research WSL, Birmensdorf, Switzerland, [3]Department of Earth and Space Sciences, Southern University of Science and Technology, Shenzhen, China, [4]Department of Civil Engineering, The University of Hong Kong, Pokfulam, Hong Kong SAR, China

Key Points:

- Granular flow mobility exhibits a non-monotonic dependence on the proportion of large particles
- Seismic signals exhibit a two-segment positive correlation with the Savage number and collisional stress across flow regimes
- A dimensionless amplitude parameter unifies the relationship with the Savage number independent of flow regime

Supporting Information:

Supporting Information may be found in the online version of this article.

Correspondence to:

Y. Cui,
yifeicui@mail.tsinghua.edu.cn

Citation:

Zhou, X., Cui, Y., Zhang, Z., Ye, L., & Fang, J. (2025). Linking dynamic parameters and seismic signals of granular flows in different flow regimes: An experimental assessment of effects of particle composition. *Journal of Geophysical Research: Earth Surface*, *130*, e2025JF008354. https://doi.org/10.1029/2025JF008354

Received 7 FEB 2025
Accepted 19 SEP 2025

Author Contributions:

Conceptualization: Xinzhi Zhou, Yifei Cui
Data curation: Xinzhi Zhou
Formal analysis: Xinzhi Zhou, Yifei Cui, Zhen Zhang, Jun Fang
Funding acquisition: Yifei Cui, Lingling Ye
Investigation: Xinzhi Zhou, Jun Fang
Methodology: Xinzhi Zhou, Jun Fang
Project administration: Yifei Cui
Resources: Xinzhi Zhou
Software: Xinzhi Zhou
Supervision: Yifei Cui
Validation: Xinzhi Zhou, Zhen Zhang, Lingling Ye, Jun Fang
Visualization: Xinzhi Zhou
Writing – original draft: Xinzhi Zhou
Writing – review & editing: Yifei Cui, Zhen Zhang, Lingling Ye

Abstract Geophysical flows, governed by particle composition and channel slope, exhibit distinct kinematic properties and seismic responses under different flow regimes. This study examines the impact of particle composition on granular flow dynamics and seismic signal generation under various flow regimes using flume experiments under dam break conditions. By varying particle composition and flume inclination angles, we investigate the kinematic properties, seismic responses, and the relationship between flow regimes and seismic signal characteristics. The results reveal that particle composition significantly affects flow dynamics, with peak velocity exhibiting a non-monotonic dependence on particle size, and an optimal proportion of large particles maximizing mobility. Seismic signals, including peak amplitude and power spectral density, increase with larger particle sizes and steeper inclination angles, indicating a strong coupling between flow dynamics and seismic responses. A two-segment positive correlation between seismic signals and collisional stress highlights the role of flow regimes, with particle-ground impacts during intense collisional interactions dominating seismic signal generation, we then introduce a dimensionless amplitude parameter and establish a unified correlation with the Savage number across flow regimes. This study advances the understanding of granular flow dynamics and seismic signatures, providing a framework for interpreting seismic data in debris flow monitoring and hazard assessment. Future work to explore the interplay of frictional and collisional mechanisms to refine models of granular flow behavior and physical interpretation of seismic data is warranted.

Plain Language Summary Debris flows and landslides can rapidly descend slopes, posing significant hazards. Their movement is influenced by the slope's gradient and the size and type of particles within the flow. In this study, we used laboratory experiments to explore how different mixtures of small and large particles affect the speed of the flow and the shaking of the ground caused by the moving material. We found that flows containing both small and large particles can move faster than flows with only one particle size. The shaking of the ground, which creates seismic signals, becomes stronger and shows more high-frequency vibrations when larger particles are present or when the slope is steeper. Different types of flow behavior, such as when particles mainly collide or slide, also change the shaking patterns. We developed a new parameter to better link the strength of the seismic signals with how the flow moves. These findings help scientists better understand how debris flows behave and how to monitor them using seismic signals to improve hazard prediction.

1. Introduction

Debris flows are complex mixtures of water, clay, and coarse particles such as boulders, exhibiting diverse macroscopic behaviors ranging from high-concentration fine-grained flows to particle suspensions and cohesive aggregates resembling concrete (Iverson, 1997; Jaeger and Nagel, 1992; Pierson, 1981; Takahashi, 2014). The composition of particles significantly influences the flow dynamics by affecting soil structure, pore water pressure, and rheological properties, resulting in various flow regimes (Iverson, 1997). The particle size distribution in debris flows ranges broadly from clay-sized particles (<2 μm) to boulders with diameters of 1–10 m (Bardou et al., 2003). This leads to distinct flow characteristics, such as coarse particles segregating to the surface (Stock and Dietrich, 2006; Takahashi et al., 1992) and fine particles suspending within the pore fluid (Iverson, 1997; Pierson, 1981). Fine particles increase pore pressure, act as a liquid phase, and thus enhance fluid density (Mcardell et al., 2006) and viscosity (Chalk et al., 2021) while reducing particle friction (Sakai

et al., 2019). The broad particle size and composition distribution introduces complexities, as particles can behave as solids or liquids during flow, influencing particle-particle, particle-fluid, and fluid-fluid interactions and leading to friction- or collision-dominated regimes (De Haas et al., 2015, 2021; Song and Choi, 2021; Yan et al., 2023; Zheng et al., 2022). While prior studies have extensively examined the effects of particle composition on flow regimes (Forterre and Pouliquen, 2008; Iverson, 1997; Tripathi and Khakhar, 2011), understanding how flow regimes influence seismic signal generation remains critical for improving the use of seismic observation to infer debris flow dynamics.

The development of environmental seismology has revealed that debris flows generate surface vibrations detectable by seismic networks and instruments (Burtin et al., 2008; Cook & Dietze, 2022). Analyzing the mechanisms of seismic wave generation from debris flow provides insights into the physical and dynamic characteristics of debris flows (Farin, Tsai, et al., 2019), aiding in hazard early warning (Chmiel et al., 2021; Cui et al., 2024; Zhou et al., 2024, 2025a). Debris flow seismic signals primarily originate from interactions between solid particles and the bed (Farin, Tsai, et al., 2019; Tsai et al., 2012; Zhang et al., 2021b). In natural debris flows, the dense solid phase—composed of a wide range of particle sizes—tends to concentrate near the flow base, exerting sustained forces on the bed and forming granular clusters, defined here as localized, densely packed groups of interacting solid particles that collectively transmit stress within the flow body (McCoy et al., 2013; Zhang et al., 2019). The statistical properties of these transmitted basal stresses are primarily governed by the flow velocity and particle size distribution (Choi & Song, 2023). Due to size segregation, coarser particles may subsequently accumulate at the surface of these clusters during flow evolution (Jing et al., 2017). Understanding the movement characteristics of these clusters, including mean and fluctuating velocities (Arattano & Marchi, 2005; Iverson, 1997; Yu et al., 2021), is crucial since fluctuating velocities have the greatest impact on seismic signals. Factors such as solid phase composition, particle gradation, and channel slope influence these clusters' dynamics (Sakai et al., 2019; Yohannes and Hill, 2010). Broad particle gradation leads to larger particles migrating to the surface, altering the internal dynamics of solid clusters (Cui et al., 2022; Duan et al., 2022; Jing et al., 2017).

The seismic response mechanisms of granular clusters have been extensively investigated recently, revealing complex relationships between dynamic parameters and seismic signals. Empirical scaling laws demonstrate that initial conditions such as particle size, mass, slope angle, and aspect ratio significantly influence seismic signal characteristics (Farin et al., 2018, 2019a). High-frequency seismic signals are closely associated with bulk motion parameters, including flow depth, gravity, density, momentum, and kinetic energy, with basal force fluctuations identified as a primary excitation source (Allstadt et al., 2020). Additionally, scaling relationships between seismic power, granular temperature, mean velocity, shear rate, and inertial numbers emphasize the intricate coupling between granular dynamics and seismic responses (Arran et al., 2021; Bachelet et al., 2023). Granular fluctuations within solid clusters significantly affect seismic signal attributes. Coarse particles dominate basal dynamics due to their larger mass and higher impact forces upon collision with the bed, leading to enhanced seismic excitation through normal impacts (De Haas et al., 2021). The relationship between particle size and basal force fluctuations exhibits a nonlinear scaling with particle diameter, typically following a $D_e^{1.5}$ relation (Farin, Tsai, et al., 2019; Zhang et al., 2021b), indicating that larger particles disproportionately contribute to seismic signal generation. Furthermore, as highlighted by Zhang et al. (2021a), coarse particles tend to organize into strong force chains within the granular flow, allowing internal stresses to be efficiently transmitted to the bed, thereby amplifying the basal stress fluctuations responsible for high-frequency seismic signals. These recent investigations highlight the critical role of granular dynamics in seismic signal generation; however, the impact of flow regimes — particularly the transition between frictional and collisional regimes — on these mechanisms remains underexplored, posing challenges to the direct implication of debris flow dynamics using seismic data.

This study focuses on how particle composition affects granular flow dynamics and the generation of seismic signals under different flow regimes. We conducted flume experiments with uniform slopes, varying particle compositions and flume inclination angles to manipulate flow regimes. Simultaneous video recordings and seismic measurements allowed us to link seismic parameters (e.g., amplitude, Power spectral density (PSD)) with flow dynamics directly. With this simplified experimental setup, we try to address the following questions: (a) How do particle composition and flume inclination angle affect granular flow dynamics? (b) How do particle composition and flume inclination angle influence seismic signals generated by granular flows? (c) How do the relationships between granular flow dynamics and seismic signals differ across flow regimes and why?

Table 1
Experimental Conditions

f_l (%)	f_s (%)	d_s (mm)	θ (°)	$\dot{\gamma}$	N_F	N_{Sav}	Flow regime
100	0	6	20	19.52 ± 0.23	1.27 ± 0.02	0.12 ± 0.00	collisional
75	25	5	20	29.37 ± 1.10	1.91 ± 0.06	0.18 ± 0.02	collisional
50	50	4	20	36.61 ± 3.68	2.27 ± 0.18	0.20 ± 0.05	collisional
25	75	3	20	30.09 ± 1.51	1.89 ± 0.07	0.07 ± 0.01	frictional
0	100	2	20	18.46 ± 0.69	1.20 ± 0.04	0.01 ± 0.00	frictional
100	0	6	25	34.33 ± 0.98	2.30 ± 0.08	0.35 ± 0.02	collisional
75	25	5	25	41.86 ± 5.47	2.81 ± 0.29	0.37 ± 0.12	collisional
50	50	4	25	50.07 ± 3.67	3.13 ± 0.13	0.39 ± 0.10	collisional
25	75	3	25	43.76 ± 2.15	2.83 ± 0.12	0.16 ± 0.03	collisional
0	100	2	25	34.40 ± 1.30	2.34 ± 0.10	0.04 ± 0.00	frictional
100	0	6	30	48.85 ± 2.77	3.52 ± 0.14	0.65 ± 0.10	collisional
75	25	5	30	43.69 ± 1.66	3.33 ± 0.04	0.32 ± 0.04	collisional
50	50	4	30	54.96 ± 2.33	3.75 ± 0.10	0.41 ± 0.05	collisional
25	75	3	30	51.65 ± 0.20	3.53 ± 0.06	0.20 ± 0.00	collisional
0	100	2	30	43.16 ± 4.37	3.14 ± 0.25	0.06 ± 0.01	frictional

Note. Each experiment was repeated three times. f_l denotes the proportion of large particles, and f_s represents the proportion of small particles. The mean particle diameter d_s is calculated by $d_s = f_s \times d_1 + f_l \times d_2$. θ is the flume inclination angle, $\dot{\gamma}$ is the shear rate, N_F is the Froude number, and N_{Sav} is the Savage number. Values of $\dot{\gamma}$, N_F, and N_{Sav} are reported as "mean ± standard deviation" based on three repeated experiments. The standard deviations reflect experimental repeatability and computational propagation of measurement uncertainty. The flow regime of the experimental granular flow is distinguished by the Savage number: when the Savage number is less than 0.1, the flow is friction-dominated, whereas higher values indicate a collision-dominated regime. In natural debris flows, the shear rate ranges from 1 to 100 (Iverson, 1997), the Froude number ranges from 0.5 to 7.6 (Cui et al., 2015; Hübl et al., 2009; Scheidl et al., 2013), and the Savage number ranges from 10^{-7} to 1 (Iverson, 1997).

2. Materials and Methods

2.1. Experimental Setup

We conducted a series of experiments to examine the impact of debris flow composition on kinetic parameters and seismic signals, as well as the correlation between these parameters under various flow conditions. The experiments involved systematically altering the proportions of large-size glass beads (6 mm) and small-sized glass beads (2 mm), and testing at three different flume inclination angles. In order to address the impact of natural variability, each experiment was replicated three times, leading to a total of 45 sets of experiments (Table 1).

The experimental flume consisted of a 0.6 m × 0.2 m × 0.45 m particle tank with a 1.5 m long flow acceleration section and a 0.5 m long outflow section (Figures 1a and 1b). The flume inclination angle was carefully maintained at 20°, 25°, and 30° using a crane. A motorized gate at the end of the granular tank regulated the release of experimental material. The experimental materials consisted of two types of glass beads, each varying in particle size and color. One type is yellow glass beads measuring 2 mm in diameter, while the other type is red glass beads measuring 6 mm in diameter (Figure 1c). The density of all glass beads is 2,550 kg/m^3, and the Young's modulus is 74 GPa. Because of the dynamic fluctuations in the solid volume fraction of the granular flow, which are challenging to measure in real time, we relied on the bulk density and angle of internal friction measured when the experimental material was at rest as the foundation for subsequent analyses in all experimental groups. The estimated bulk density is 1,667 kg/m^3, indicating a solid volume fraction of approximately 0.65. By observing the angle formed by the collapsed pile of beads as they gradually descended onto the plate, the angle of internal friction of the beads on this plate was estimated to be approximately 17°. Based on a tilting test (detailed in Text S3 of the Supporting Information S1), the coefficient of friction between the glass beads and the flume's bottom plate is determined to be 0.25. It is acknowledged that both bulk density and friction coefficient may evolve during flow due to particle dilation and changes in dynamic friction. However, in this study, the bulk density was

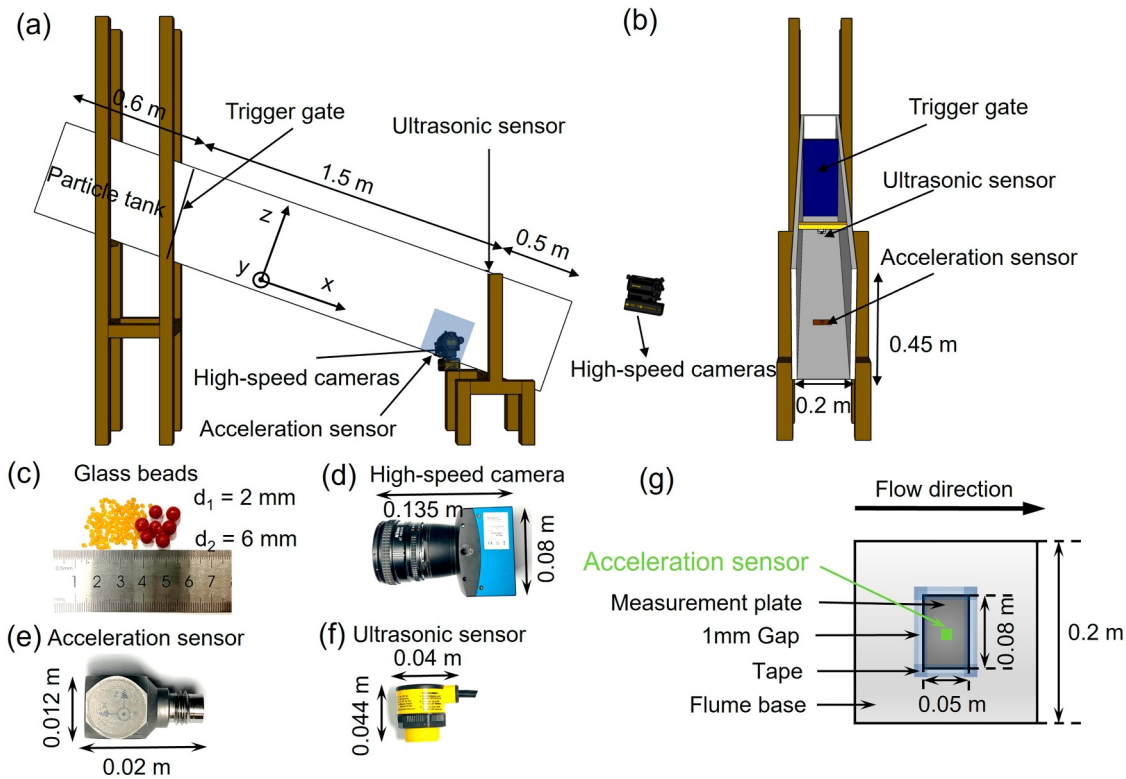

Figure 1. Schematic of experimental apparatus. (a) Front view of the experimental flume, including the 0.6 m × 0.2 m × 0.45 m particle box and the 1.5 m long flow acceleration zone, with the blue shading indicating the observation area of the high-speed camera. (b) Side view of the experimental flume with a measurement plate equipped with an acceleration sensor 1.5 m downstream of the valve and an ultrasonic sensor directly above it. (c) Photograph of the glass beads used in the experiments with particle sizes of $d_1 = 2$ mm and $d_2 = 6$ mm. (d) High-speed camera. (e) Acceleration sensor. (f) Ultrasonic sensor. (g) Schematic of the measurement plate installation with sealing tape applied in the mounting gap.

measured based on the initial packing prior to flow initiation, and the basal friction coefficient was determined via tilting tests under quasi-static conditions. These measurements provide reasonable approximations for the average material properties used in the calculation of dimensionless parameters, while dynamic effects such as transient dilation and velocity-dependent friction are considered secondary in the first-order scaling analyses presented here.

Prior to each experiment, mixtures of large- and small-diameter glass beads were precisely prepared according to the target mass fractions specified in the experimental design. The desired masses of each particle size were weighed separately using an electronic scale with a precision of ±0.01 kg. The total mixture mass was consistently maintained at 50 kg, and the prepared mixtures were subsequently deposited into the particle tank at the upstream end of the flume. The beads were then released by activating the motorized gate, causing them to cascade and flow downstream the flume, forming a continuous granular flow. To measure the seismic signals generated by the experimental granular flow, a 0.05 m × 0.08 m measurement plate was positioned 1.5 m downstream of the particle tank. A triaxial acceleration sensor (Kistler 8763B250BB, with a response frequency of 1–10000 Hz) was then placed directly beneath the plate (Figures 1b–1e). This study aimed to examine the impact of the physical properties of a seismic source on seismic signals. Specifically, it sought to emphasize the seismic signals produced by the particles above the measurement plate. Therefore, to minimize the path effect, the measurement plate was separated from the bottom of the flume by one mm, and the gap was connected with tape (Arran et al., 2021; De Haas et al., 2021). Flow depth was measured using an ultrasonic sensor (BANNER U-GAGE T30UXUA, 0.1–1.0 m, resolution 0.1% of distance) right above the measurement plate (Figures 1b–1f). The data from both the acceleration sensor and the ultrasound sensor were recorded using a data acquisition instrument (DH5902N) at a sampling rate of 25.6 kHz. This sampling frequency was selected to match the full response bandwidth of the accelerometer (1–10 kHz), ensuring accurate capture of the high-frequency components of the seismic signals associated with granular impacts (Bachelet et al., 2023). The flume was

constructed with transparent Plexiglas sidewalls, enabling a high-speed camera (Norpix FR-stream3-fiber, 1,728 × 1,504 pixels, 500 fps) to record the movement of the granular flow. These videos were then utilized to calculate the dynamic properties of the granular flow (Figures 1b–1d).

To ensure comparability with natural debris flows, despite inherent scale effects, we controlled the shear rate, Froude number, and Savage number, all of which fall within the parameter ranges typical for natural debris flows (Table 1). While inherent scale effects related to absolute particle size, flow depth, and flow duration may influence secondary flow features (De Haas et al., 2021; Iverson, 1997; Takahashi, 2007), dimensionless analysis has been widely used to bridge laboratory and field scales for debris flow dynamics (Iverson, 1997; Major and Iverson, 1999). It is worth noting, however, that the primary goal of these small-scale experiments is not to create a direct scale model of natural granular flows but rather to qualitatively elucidate how flow composition and flume inclination angle influence flow characteristics and the resulting seismic signals.

2.2. Flow Measurement Using Particle Image Velocimetry Analysis

We measured the granular flow's velocity using the Particle Image Velocimetry (PIV) technique (Thielicke and Stamhuis, 2014; Willert and Gharib, 1991). This method employs an algorithm to analyze two images captured within a specific time interval (0.002 s in the current study) in order to deduce an instantaneous velocity field. The images are divided into sub-regions, and the displacement is determined by calculating the cross-correlation function for each sub-region (White et al., 2003; Willert and Gharib, 1991). The instantaneous velocity field can be determined by calculating the ratio of displacement to the time interval between images (Figure S1a in Supporting Information S1). By calculating the average of velocities in the instantaneous velocity field in the downslope direction, we obtain the downslope mean velocity, $\langle u \rangle$. The depth-averaged mean velocity, $\langle u_d \rangle$, is obtained by calculating the average of the downslope mean velocity, $\langle u \rangle$, in the depth direction (See Text S2 for details). Given that the downslope velocity component is significantly greater than the normal velocity component (Figures S1 and S2 in Supporting Information S1), the present study exclusively considers the downslope component of velocity. We also calculated the overall average downslope velocity $\langle u_d \rangle_t$, which is the average $\langle u_d \rangle$ over the total time the granular flow was estimated from the acceleration sensor.

When the granular flow moves in a flume with a high angle of inclination, particularly at 30°, the particles in the upper part of the flow move in a splashing manner. This can result in a significant error in the flow depth measured by the ultrasonic sensor. Thus, in this study, we recalibrated the granular flow depth using the flow field acquired from PIV analysis. The depth-averaged shear rate ($\dot{\gamma}$) was calculated following Wiederseiner et al. (2011) as $\dot{\gamma} = \langle u_d \rangle / h$, where $\langle u_d \rangle$ is the downslope velocity component averaged over the vertical (flow-depth) direction within the high-speed camera's field of view, and h is the corresponding flow depth. Debris flows are classified into different flow regimes based on the stresses that govern their motion (Iverson, 1997; Savage and Hutter, 1989). The Savage number (N_{sav}) is a crucial dimensionless number in this study for characterizing the dry granular flow regime. It helps determine whether frictional or collisional stresses dominate the flow (Iverson, 1997). The N_{sav} can be calculated as follows:

$$N_{\mathrm{Sav}} = \frac{d_s^2 \dot{\gamma}^2}{\mathrm{g}h \tan \varphi}, \tag{1}$$

where d_s is the mean particle diameter, $\dot{\gamma}$ is the depth-averaged shear rate, h is the flow depth, φ is the internal friction angle of the glass beads, and g is the gravitational acceleration. When $N_{sav} > 0.1$, collisional stresses predominate over frictional stresses, and vice versa (Bagnold, 1954; Savage and Hutter, 1989). The ratio of inertial force to gravitational force, or Froude number (N_F), is frequently employed to infer the dynamic properties of debris flow (Cui et al., 2015; Zheng et al., 2022). The N_F is defined as

$$N_{\mathrm{F}} = \frac{\langle u_d \rangle}{\sqrt{\mathrm{g}h \cos \theta}}, \tag{2}$$

where θ is the flume inclination. Based on the temporal evolution of the granular flow depth and flow velocity determined by PIV analysis, we estimate the potential energy loss E_p and kinetic energy E_k of the granular flow from the particle tank to the measurement plate.

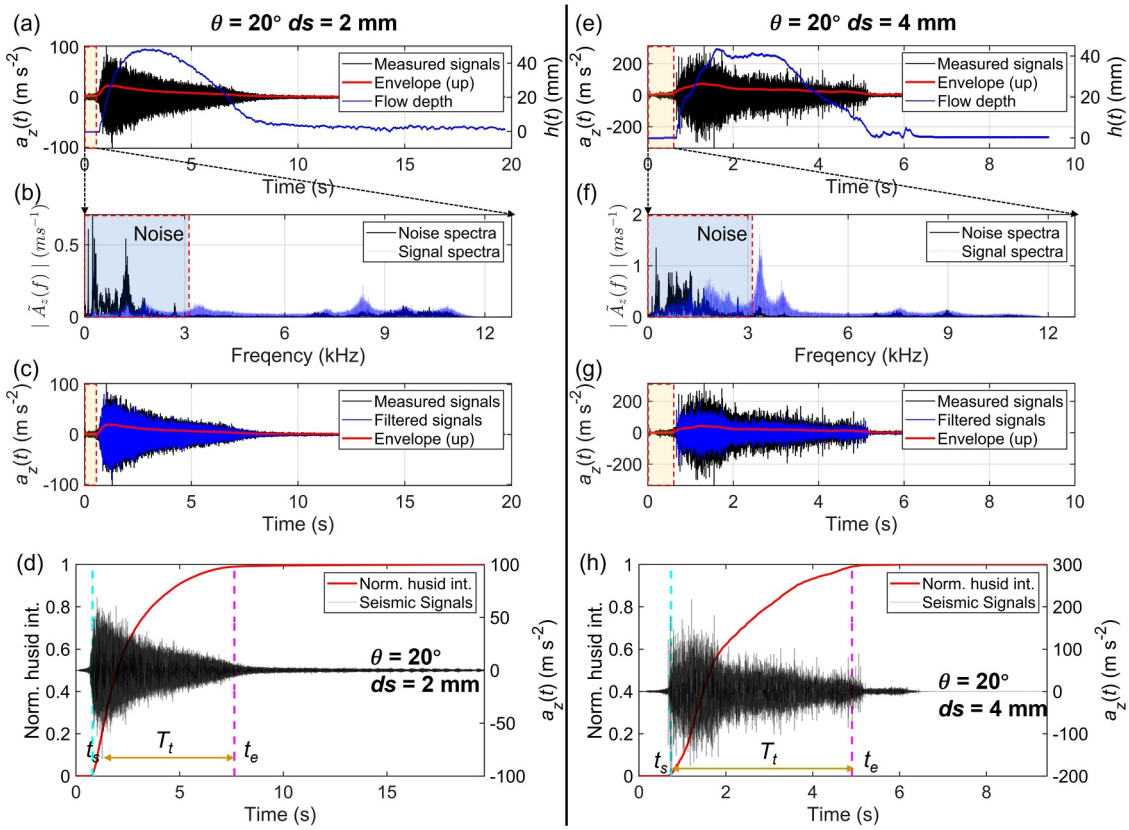

Figure 2. Sample analysis of seismic signals. (a, e) Measured seismic signals, envelopes, and flow depths over time, with the yellow shaded area marking the noise analysis period (before the granular flow reaches the measurement plate). (b, f) Noise signal spectra, with the blue shaded area highlighting dominant apparatus resonance and ambient noise. (c, g) Measured seismic signals, band-pass filtered signals (3–10 kHz), and corresponding envelopes. (d, h) Husid plots and seismic signal duration T_t derived from seismic acceleration data, with indigo and magenta dashed lines indicating start and end times, respectively.

$$E_{\mathrm{p}} = mgH = \int_{\Delta t} \rho W h \langle u_d \rangle \, g H \mathrm{d}t, \tag{3}$$

$$E_{\mathrm{k}} = \frac{1}{2} m \langle u_d \rangle^2 = \int_{\Delta t} \frac{1}{2} \rho W h \langle u_d \rangle^3 \mathrm{d}t, \tag{4}$$

where Δt is the time period for which the energy is calculated, ρ is the bulk density of experimental materials, W is the width of the measurement plate, and H is the height difference from the center of mass of the experimental materials stacked in the particle tank to the measurement plate.

2.3. Seismic Signal Data Processing

We estimated the dominant frequency band of the seismic noise by conducting spectral analysis on the recorded vertical acceleration signals before the granular flow reached the measurement plate (Figures 2a and 2e). The noise signals primarily fell within the 0–3 kHz range (Figures 2b and 2f), which may result from ambient vibrations or structural resonance of the flume. To minimize these low-frequency interferences, we applied a band-pass filter using a third-order Butterworth design with a passband of 3–10 kHz to all seismic records (Figures 2c and 2g). The acceleration signals were recorded at a sampling rate of 25.6 kHz. Baseline correction was applied to remove low-frequency drift. Instrument response correction was not applied, as the accelerometer used in our experiments was factory-calibrated and exhibited a flat frequency response over the 3–10 kHz band, which encompasses the filtered seismic frequency content used in our analysis. Amplitude was pre-corrected by the manufacturer with a fixed gain factor of 1.0, ensuring reliable amplitude fidelity. PSD was computed using Welch's method in MATLAB. These processing steps ensured that the seismic signals reflected the dominant

high-frequency components associated with granular impacts and flow dynamics while suppressing noise due to flume resonance and environmental disturbances.

To characterize the seismic signals associated with granular flow dynamics, we explored several seismic parameters using the filtered acceleration data $a_z(t)$ for various experimental setups. The start and end times of the seismic waveform, t_s and t_e, are determined by identifying the 1% and 99% limits of the Husid integral ($H_u(t)$) (Boore & Thompson, 2014; Saló et al., 2018) defined as

$$H_u(t) = \int_{t=0}^{t_{\text{final}}} a_z(t)^2 \mathrm{d}t, \tag{5}$$

where t_{final} is the end of the measurement time window. The seismic signal duration T_t, calculated as $T_t = t_e - t_s$, indicates the total time the granular flow passes through the measurement plate (Figures 2d and 2h). In our setup, the acceleration sensor's proximity, isolation of the measurement plate, and signal filtering minimize propagation-related distortions and site effects, such as reflections and resonance within the flume structure. As a result, the seismic signal duration T_t closely approximates the granular flow duration, allowing us to reliably use T_t to represent the flow motion duration (Farin et al., 2018). We calculated the root mean square (RMS) envelope of the filtered acceleration and identified its maximum amplitude using the peak value of the RMS envelope (A_p). We also determined the predominant frequency of the seismic signal (f_p) using spectral analysis. The centroid frequency (f_c), known as the mean frequency or spectral centroid, is less sensitive to the signal-to-noise ratio compared to the predominant frequency f_p (Farin et al., 2018; Lin et al., 2022). f_c is calculated by

$$f_c = \frac{\int_0^{+\infty} |\tilde{A}_z(f)| f \mathrm{d}f}{\int_0^{+\infty} |\tilde{A}_z(f)| df}, \tag{6}$$

where $|\tilde{A}_z(f)|$ is the Fourier amplitude spectrum of the filtered acceleration $a_z(t)$. The impact-force signal is transformed into a joint time-frequency domain using the short-time Fourier transform method to quantify the characteristics of the force signal (Yan et al., 2023). The frequency-dependent PSD $PSD(f)$ in each time window is calculated from the amplitude spectrum of the acceleration signal at each frequency:

$$PSD(f) = \frac{|\tilde{A}_z(f)|^2}{\Delta f}, \tag{7}$$

where Δf is the frequency resolution, which equals $1/T$ (T is the window length) in the fast Fourier analysis. The $PSD(f)$ was then averaged over frequencies above 3 kHz (after high-pass filtering) to obtain the average PSD $\overline{PSD}$ for the given time window. Following the diffuse field theory for granular impacts (Bachelet et al., 2023; Farin et al., 2016), which assumes multiple scattering and equipartition of vibrational energy within the measurement plate, the radiated elastic energy during the time period Δt (W_{el}) can be calculated using the normal velocity of the plate $v_z(t)$, directly integrated from the filtered acceleration $a_z(t)$ over time by:

$$W_{el} = M\gamma_p v_g \times \int_{\Delta t} v_z^2(t)\, \mathrm{d}t, \tag{8}$$

where M is the mass of the measurement plate, γ_p is its average viscoelastic attenuation, and v_g the average group velocity of the radiated acoustic waves (A_0 Lamb waves). The average radiated elastic power over duration Δt is determined by $\Pi_{el} = W_{el}/\Delta t$.

To quantify the measurement uncertainty, each experimental condition was repeated three times. All reported values (e.g., flow velocity, signal amplitude) represent the mean of three trials. The associated error bars correspond to the standard deviation among these repetitions, reflecting the experimental repeatability under identical setup and flow conditions.

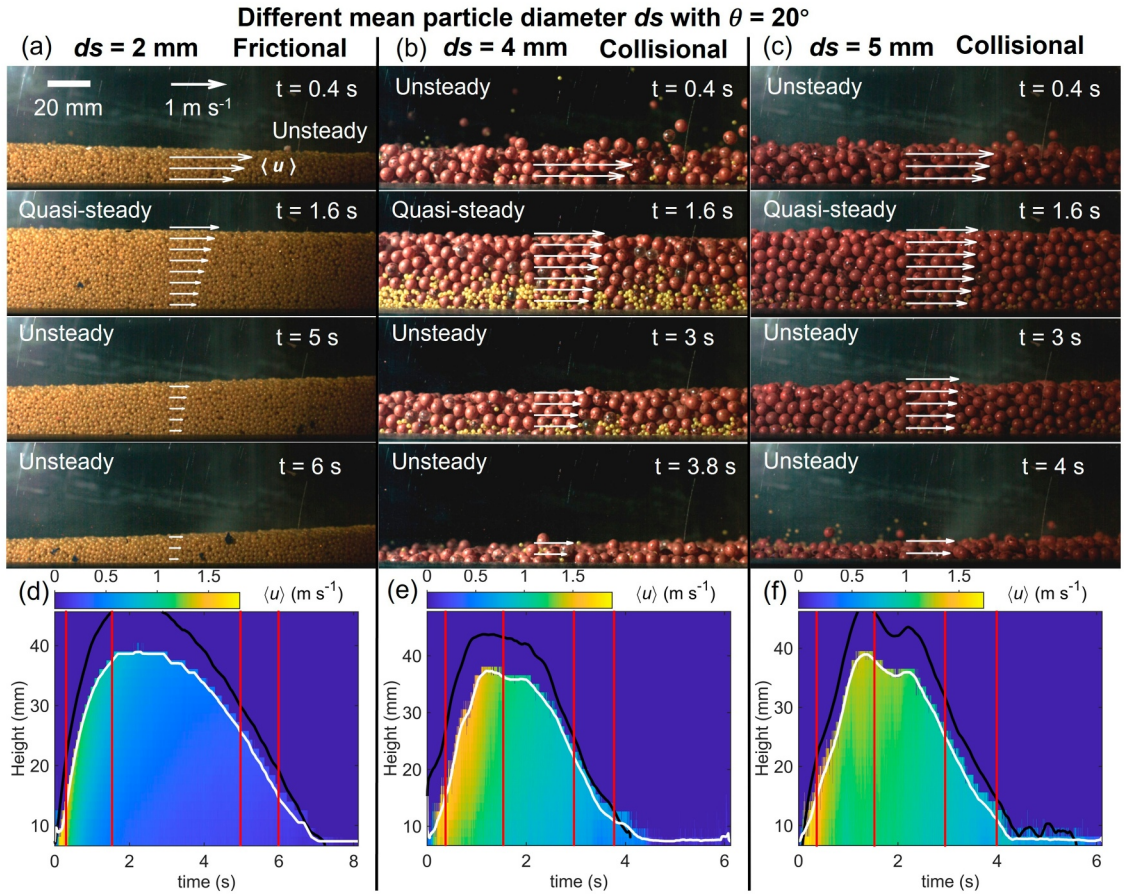

Figure 3. (a–c) Snapshots showing the main bodies of the granular flows with different mean particle diameters d_s and the flume inclination angle θ of 20°. Mean velocity profiles within the observation area calculated by Particle Image Velocimetry (PIV) are marked in each subfigure with white arrow lines. (d–f) Evolution of the mean downslope flow velocity profile $\langle u \rangle$ calculated by PIV over time. The black and white lines show the heights of the granular flow measured by the ultrasonic sensor and PIV, respectively. The vertical red lines indicate the timing of the four snapshots in (a–c).

3. Results

3.1. Observations of Granular Flow Behavior

The particle masses quickly spread and accelerated as they moved downward along the inclined flume released from the particle tank. In the side view, the flow transitions from unsteady to quasi-steady and then back to unsteady flow, reflecting changes in flow behaviors including variations in velocity, flow depth, front leap dynamics, and transitions between frictional and collisional regimes (Figures 3 and 4). Specifically, Figures 3a–3d depict overall frictional flow characteristics with the flume inclination angle of 20°. At $t = 0.4$ s, the granular flow exhibits high speed and shallow depth in the leading edge section. At $t = 1.6$ s, the flow depth increases rapidly while the flow velocity decreases. During this time, the particles become densely packed, and the granules are less agitated in the main body. Afterward, particle collisions lead to heightened agitation in the main body (at $t = 5.0$ s), reflecting more dispersive and less cohesive flow behaviors, and followed by a sharp decline in both the velocity and depth of the particle flow (at $t = 6.0$ s). At the trailing edge of the granular flow, the flow appears more dispersed with a lower volume fraction (as shown in the last panel of Figures 3a–3c). It was observed when the volume fraction of particles at the leading and trailing edges was lower than in the main body (Figures 3a–3c). Such propagated behaviors were observed consistently across all experiments in this study. In the experiments involving mixed particle sizes (Figures 3b and 3c), the upper layer and leading edge of the granular flow held a relatively high concentration of large particles (6 mm) and small particles (2 mm) dominated the bottom layer and rear sections of the flow, indicating the occurrence of particle size segregation as the flow progressed.

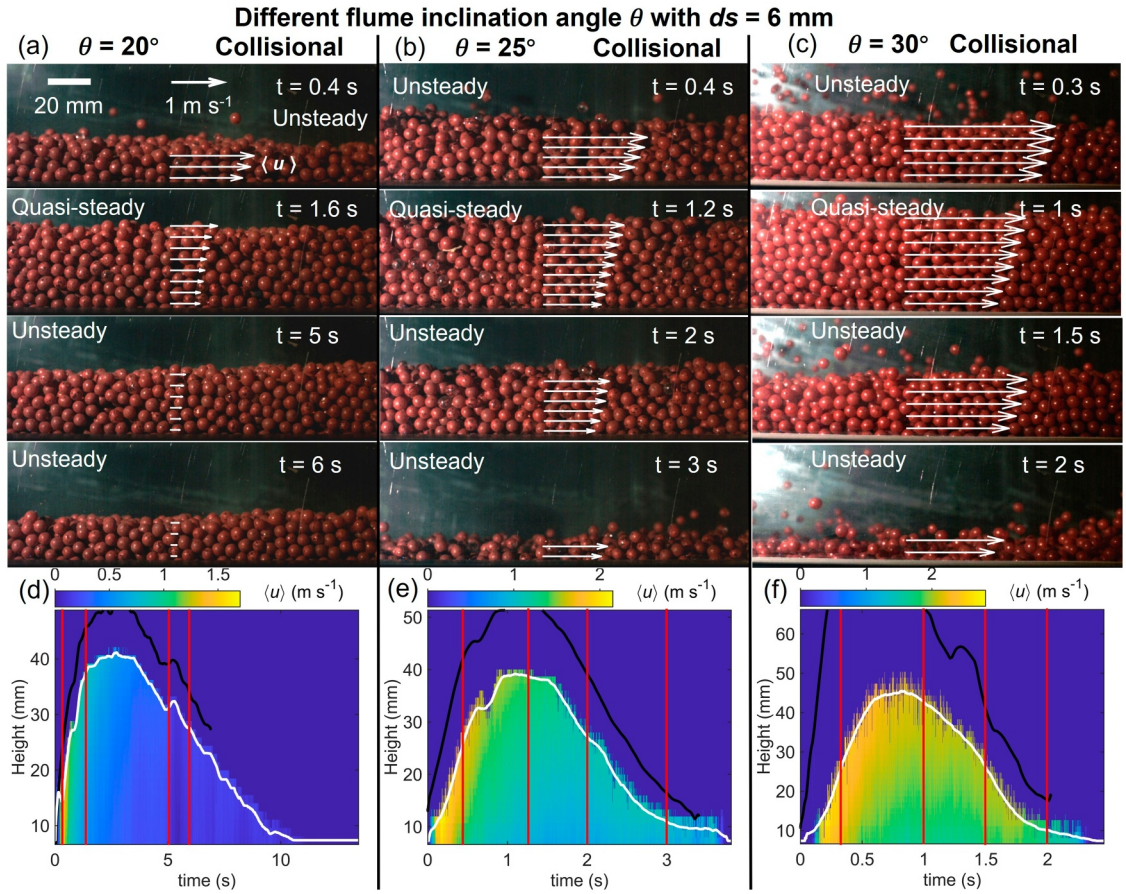

Figure 4. (a–c) Snapshots showing the main bodies of the granular flows with different flume inclination angle θ and fixed d_s = 6 mm. Mean flow velocity profiles within the observation area calculated by Particle Image Velocimetry (PIV) are marked in each subfigure with white arrow lines. (d–f) Evolution of the mean downslope flow velocity profile $\langle u \rangle$ calculated by PIV over time. The black and white lines in the figure indicate the height of the granular flow measured by the ultrasonic sensor and PIV, respectively. The vertical red lines indicate the timing of the four snapshots in (a–c).

The variations in flow velocity across the leading edge, main body, and trailing edge of the granular flow are influenced by particle composition and flume inclination angle. For experiments with a flume inclination angle of 20° but varying particle compositions, the leading edge velocity of all granular flows remains approximately 1.7 m/s (Figure S3d in Supporting Information S1). For the main body, the velocity initially increases and then decreases with the increase in the mean particle diameter, reaching a peak of 1.3 m/s at d_s = 4 mm. The trailing edge shows a similar velocity trend. Flow depth remains largely unaffected by changes in particle size, possibly due to that the shear rate of the main body of the granular flow may also increase and then decrease with increasing mean particle diameter as indicated by the trend of flow velocity profiles. The spatial distribution of particles on the flow surface becomes more scattered as the mean particle diameter varies, reaching its maximum heterogeneity at d_s = 4 mm (Figures 3a–3c). The observed non-monotonic variation of flow velocity with mean particle size is consistent with previous studies showing that particle-size-induced packing efficiency affects bulk flow mobility, where mixtures of large and small particles initially enhance flowability but eventually lead to jamming and reduced mobility at higher large-particle contents (De Haas et al., 2021; Yohannes and Hill, 2010).

The snapshots and evolution of the mean downslope velocity profile of granular flows over time for tests with varied flume inclination angles and fixed d_s = 6 mm are displayed in Figure 4. With increased inclination angles, the transition to the collisional flow leads to more frequent and energetic particle-particle collisions accompanied by high velocity fluctuations. The high-speed camera video provides a clear overview of the granular flow process, distinguishing between the highly dispersed leading and trailing edges and the dense main body (Figures 4a–4c). In the θ = 30° case, the collisional flow regime is evident with visibly agitated particles even within the main body. The high-speed camera videos provide a clear visualization of the granular flow processes,

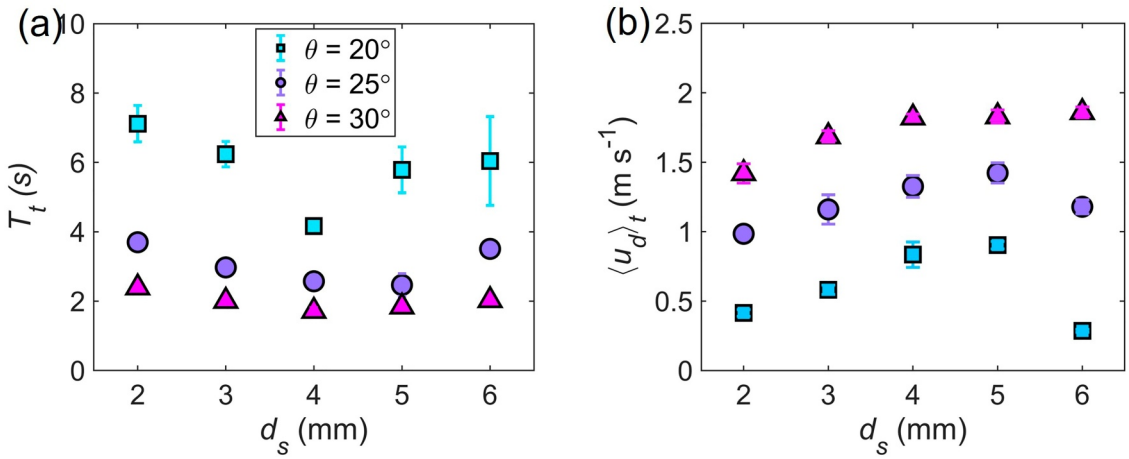

Figure 5. Variation of duration T_t (a) and overall average downslope velocity $\langle u_d \rangle_t$ (b) with mean particle diameters for flume inclination angles of 20° (squares), 25° (circles) and 30° (triangles). The error bars in (a) indicate the standard deviation of duration calculated from repeated experiments.

revealing distinct regions of the leading edge, main body, and trailing edge (Figures 4a–4c). As the flume inclination angle increases, the flow transitions toward a more collisional regime, evidenced by more agitated particle motions within the main body, particularly at $\theta = 30°$. The flow velocity increases with steeper inclination angles, as shown by the higher average velocities in Figures 4d–4f and S4(d). From high-speed video and PIV measurements, the leading-edge velocity reaches approximately 2.7 m/s, while the main body velocity reaches ∼2.1 m/s at $\theta = 30°$. Meanwhile, flow depth shows a general decreasing trend with increasing inclination angle (black lines in Figures 4d–4f). The enhanced particle agitation results in stronger velocity fluctuations and elevated shear rates (Figure 4 and S4). In addition, the total flow duration decreases markedly from ∼11 s at $\theta = 20°$ to less than 3 s at $\theta = 30°$ (Figures 4d–4f), reflecting the increased flow mobility under higher inclination conditions.

3.2. Dynamic Parameters

Dynamic parameters of the granular flow, the duration T_t and the overall average downslope velocity $\langle u_d \rangle_t$, are influenced by the composition and flume inclination angle. As shown in Figure 5a, the duration, decreasing with the flume inclination for the fixed distance, is shortest when the mean particle diameter is 4 mm (50% proportion of large particles). The measured depth-averaged mean velocity $\langle u_d \rangle_t$ is inversely proportional to the duration T_t as expected, and the largest $\langle u_d \rangle_t$ was slighted shifted with a mean particle diameter of 4 mm or 5 mm for different inclination angles (Figure 5b). The mixture of different particle sizes, particularly with a moderate proportion of large particles, enhances flow mobility due to size segregation effects: large particles preferentially migrate to the surface while small particles fill the lower layers, thereby reducing internal friction and enhancing packing stability, which collectively facilitate higher mean flow velocities and shorter durations (Kokelaar et al., 2014).

The temporal variation of the dynamic characteristics is compared for different mean particle diameters d_s and different flume inclination angles θ in Figure 6. The increase in the proportion of larger particles leads to enhanced flow mobility, reflected in higher depth-averaged velocities across various inclination angles (Figures 6a–6d and 6g). The granular flow's maximum depth-averaged velocity is found at its leading edge, and interestingly, this maximum velocity remains unaffected by the mean particle diameter. The depth-averaged velocities of the main body exhibited a non-monotonic dependence on mean particle diameter, with an optimal proportion of large particles yielding the highest flow velocity. The velocity of the granular flow increases noticeably as the flume's inclination angle increases. The flow depth increases rapidly with the arrival of the granular flow, reaching a maximum in the main body before gradually decreasing (Figure 6b, 6e, 6h). The mean particle diameter and flume inclination angle have minimal impact on the evolution of the flow depth, particularly the maximum value. The shear rates at the leading and trailing edges of the granular flow are considerably larger compared to those in the central part by a factor of 3–8 (Figures 6c, 6f and 6i). This suggests that the particles at the edges are widely dispersed and highly active, resulting in fluctuations in the shear motion between the granular layers. On the other hand, the particles in the main body are densely packed and the shear rate remains consistent, which aligns with

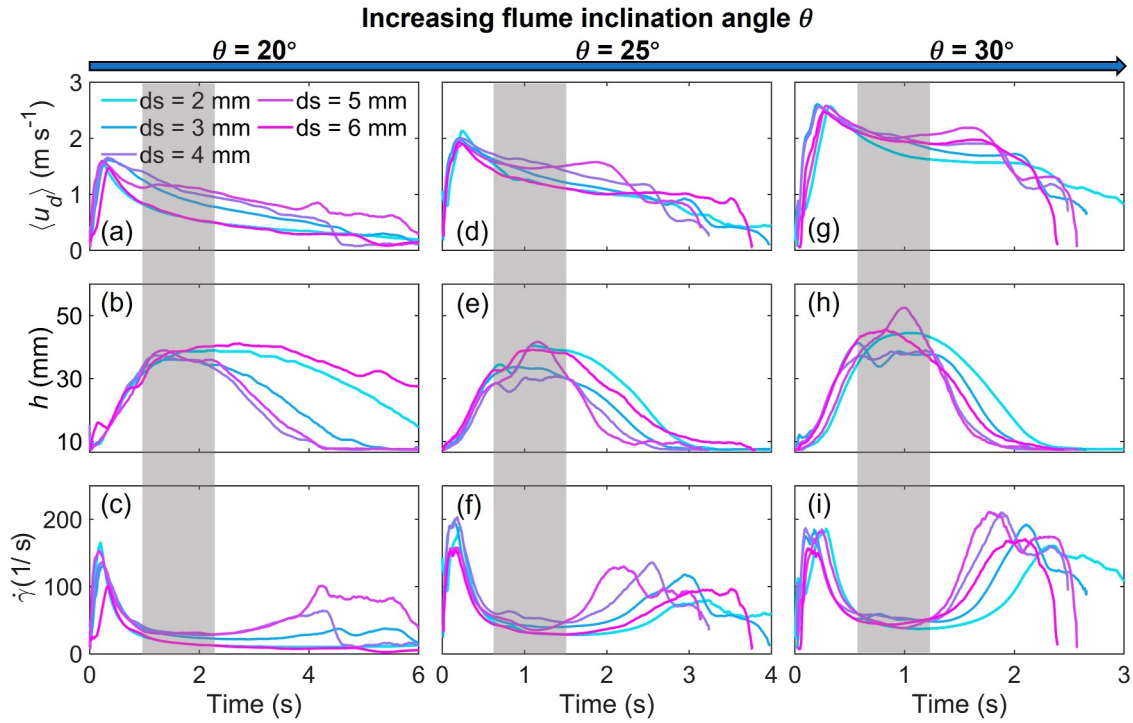

Figure 6. Variations of depth-averaged velocity $\langle u_d \rangle$, flow depth h and shear rate $\dot{\gamma}$ as a function of time for the flume inclination angles of 20°, 25°, and 30°. The shaded areas indicate the quasi-steady state with nearly constant shear rate (c, f, i).

the images captured by the high-speed camera (Figures 3 and 4). Thus, we define the quasi-steady state as the period within the main body of the flow during which the depth-averaged velocity $\langle u_d \rangle$ and flow depth h vary gradually without abrupt fluctuations, and the shear rate $\dot{\gamma}$ remains within ±10% variation over three consecutive 0.1 s sliding time windows. Based on this criterion, a representative duration of 0.6 s was selected for parameter extraction and seismic signal analysis.

We find that the peak of the downslope depth-averaged mean velocity $\langle u_d \rangle_p$ is influenced by the mean particle diameter and flume inclination angle (Figure 7). $\langle u_d \rangle_p$ shows a consistent increase with the flume inclination angle as expected. The variation of $\langle u_d \rangle_p$ with the particle size follows a non-monotonic trend, initially increasing and then decreasing with the peak at the mean particle dimension of ~4 mm. The values of highest $\langle u_d \rangle_p$ are 1.2 m/s, 1.6 m/s, and 2.2 m/s for flume inclination angles of 20°, 25°, and 30°, respectively. The maximum flow depths show little variation for all cases with average value ~40 mm (Figure 7b). The variations of shear rate $\dot{\gamma}$ and Froude number N_F with the mean particle size and inclination angle exhibit similar non-monotonic trends as observed for the maximum depth-averaged flow velocity (Figures 7c and 7e). The normalized downslope depth-averaged mean velocity $\langle u_d \rangle_p / (g d_s)^{0.5}$ generally decreases with increasing particle size, while at 20°, a non-monotonic trend is observed, with the normalized velocity initially increasing and then decreasing (Figure 7d). The Savage numbers N_{sav} of all cases range from 0.01 to 1, falling within the range of N_{sav} typically observed in natural debris flows from 10^{-7} to 1 (Iverson, 1997; Iverson and Denlinger, 2001; Zhou and Ng, 2010). Most of the experimental granular flows observed are collisional with $N_{sav} > 0.1$, with only a few cases being frictional with relatively small mean particle diameters of 2–3 mm (Figure 7f).

3.3. Seismic Parameters

We observe distinct seismic behaviors between frictional and collisional flows (Figure 8). In frictional flows with a mean particle diameter of 2 mm, as the leading edge of the granular flow reaches the measurement plate, the seismic signal amplitude shows a gradual increase (Figure 8a), which coincides with the increase in flow depth and velocity observed in the velocity and depth measurements (Figure 3d). In contrast, the leading edge impact generates a sharper and higher amplitude spike in collisional flows due to intense particle collisions (Figures 8d and 8g). The main body of the frictional flow generates a relatively stable seismic signal with minimal

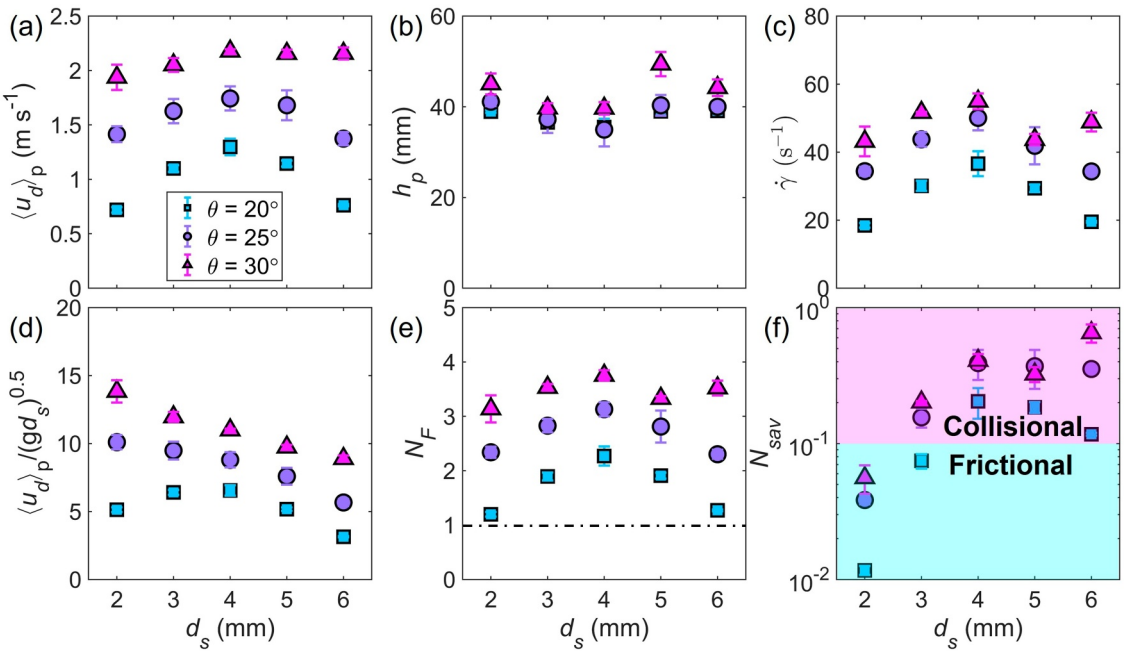

Figure 7. Effects of mean particle diameters d_s and flume inclination angle θ on the flow dynamic parameters: (a) Peak downslope depth-averaged mean velocity $\langle u_d \rangle_p$, (b) peak flow depth h_p, (c) shear rate $\dot{\gamma}$, (d) normalized downslope depth-averaged mean velocity $\langle u_d \rangle_p / (g d_s)^{0.5}$, (e) Froude number N_F and (f) savage number N_{sav}.

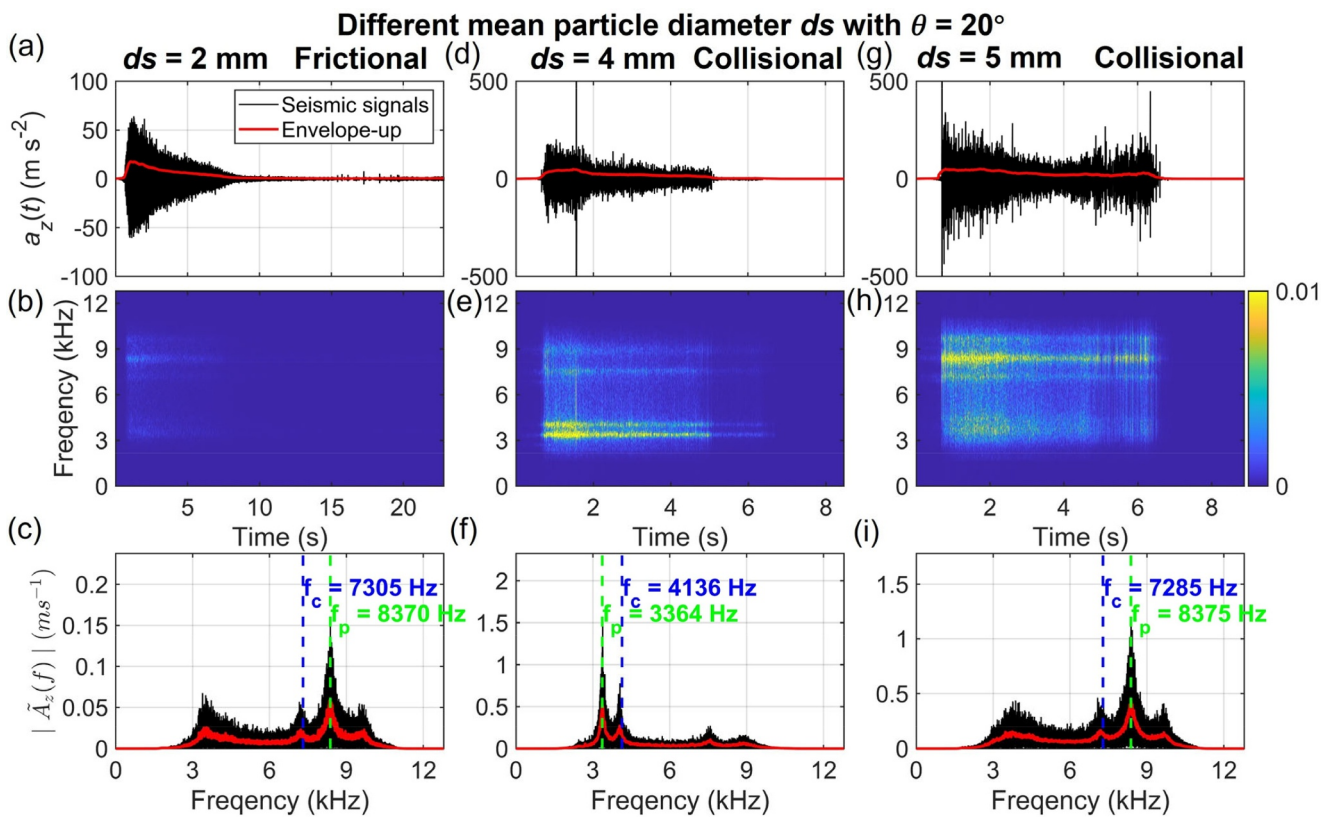

Figure 8. Examples of (a, d, g) seismic signals generated by the granular flows with red curves showing envelops, (b, e, h) spectrograms of the signals, and (c, f, i) spectrums of the seismic signals with red curves showing a smoothing characteristic of the Fourier spectra with a window of 150 samples. The inclination angle is 20°. The left, middle and right panels are experiments with mean particle diameters of 2, 4, and 5 mm, respectively.

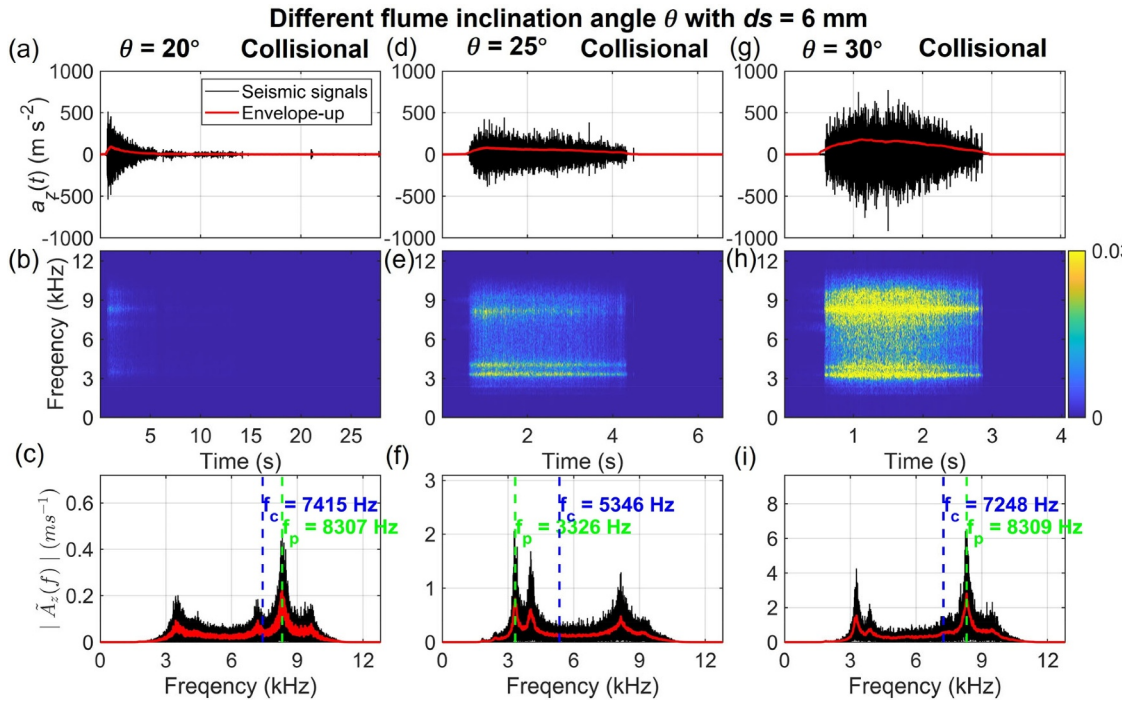

Figure 9. Examples of (a, d, g) seismic signals generated by the granular flows with red curves showing envelops, (b, e, h) spectrograms of the signals and (c, f, i) spectrums of the seismic signals with red curves showing a smoothing characteristic of the Fourier spectra with a window of 150 samples. The mean particle diameter is 6 mm. The left, middle and right panels are for inclination angles of 20°, 25°, and 30°, respectively.

fluctuations, indicative of cohesive particle motion. In contrast, collisional flows exhibit a more fluctuating seismic signal due to frequent particle interactions. The trailing edge causes a gradual decrease in seismic amplitude in both flow types, though collisional flows may show a more abrupt amplitude decay (Figure 8g). Notably, in certain collisional flow cases, a gradual and accelerated increase in seismic signal amplitude is observed at the trailing edge, likely associated with enhanced saltation and dispersion of particles (e.g., Figure 8g). This phenomenon is less prominent in frictional flows due to lower particle agitation.

As the mean particle diameter d_s and flume inclination angle θ increase, the seismic signal amplitude grows (Figures 8 and 9 and S5). The spectrograms reveal that the seismic signals generated by the granular flow exhibit a direct correlation with both d_s and θ. The energy is predominantly concentrated within the frequency bands of 3.1–3.5 kHz and 8.1–8.5 kHz (Figures 8 and 9).

Figure 10 shows that the seismic signals generated by the experimental granular flows exhibit larger peak amplitude A_p, peak PSD PSD, radiated elastic energy W_{el} and radiated elastic power Π_{el}, which increase with both the flume inclination angle and the mean particle diameter. Across both flow regimes, A_p, PSD, W_{el}, and Π_{el} increase as d_s rises from 2 to 4 mm, followed by a more gradual increase at larger d_s (Figure 10a–10d). The frequency centroid f_c displays an initial decrease followed by a subsequent increase as the mean particle diameter d_s increases (Figure 10e), and the predominant frequency f_p exhibits fluctuations around 3.35 kHz or 8.350 kHz with little variation with d_s and θ (Figure 10f) for both frictional and collisional flows. As d_s and θ increase, the W_{el}/E_p ratio grows, indicating that a greater proportion of lost potential energy E_p being converted to radiated elastic energy W_{el}. This effect is particularly pronounced in collisional flows, where W_{el}/E_p can reach up to 4.7×10^{-5} (Figure 11).

3.4. Comparison of the Seismic and Dynamic Parameters

In order to better understand which flow dynamic parameters have the most influence on the generated seismic signal, we compare the peak amplitude A_p of the seismic signal with some dynamic parameters. Our experiments consistently demonstrate a positive correlation between A_p and variables $\langle u_d \rangle_p$, h_p, and $\dot{\gamma}$, albeit with relatively small correlation coefficients R^2 from 0.2 to 0.52 (Figure 12). The relatively weak correlations are likely due to

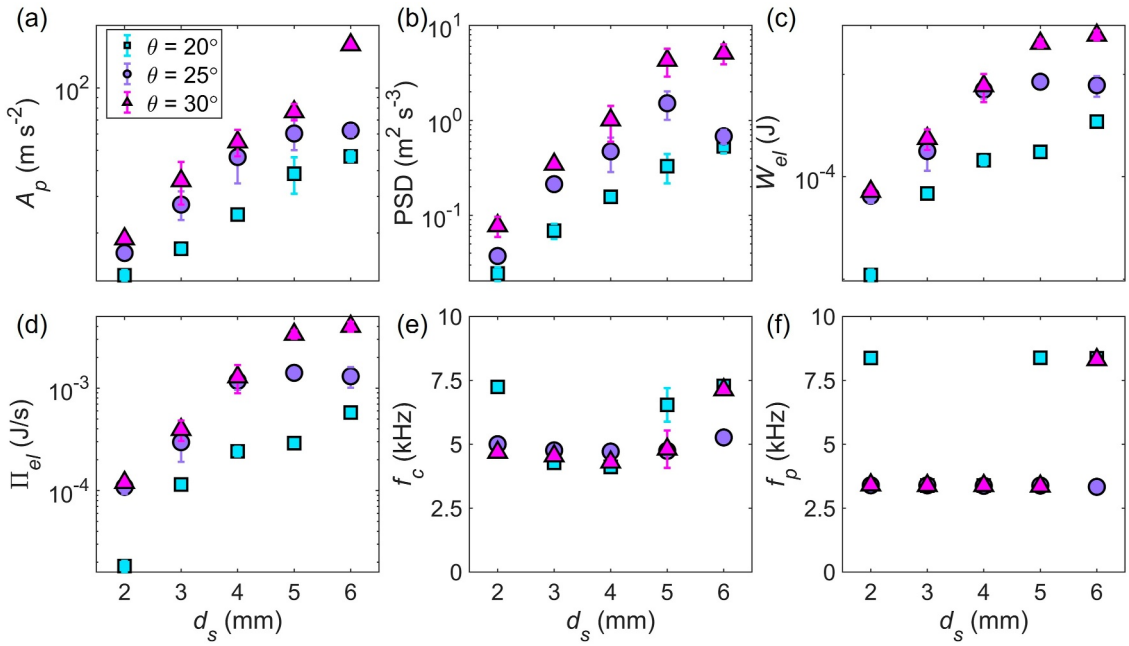

Figure 10. Effects of mean particle diameters d_s and flume inclination angle θ on the seismic parameters: (a) Peak amplitude A_p, (b) peak power spectral density PSD, (c) radiated elastic energy W_{el}, (d) radiated elastic power Π_{el}, (e) centroid frequency f_c and (f) predominant frequency f_p of seismic signals generated by experimental granular flows.

the combined influence of multiple flow characteristics, such as flow width, flow depth, flow velocity, and grain size on the resulting signal (Farin, Tsai, et al., 2019; Lai et al., 2018). Previous attempts to correlate seismic amplitudes with only a single flow parameter have not yielded consistent patterns (Lavigne et al., 2000).

Dimensional analysis, guided by Buckingham's Π theorem, provides a systematic framework for identifying independent dimensionless variables by analyzing the fundamental units involved in a physical system (Iverson, 2015). This study allows the reduction of multiple governing parameters—such as flow depth, velocity, particle size, and gravitational acceleration—into key dimensionless groups such as the Froude number, Savage number, and normalized seismic parameters, facilitating comparisons across different flow conditions and regimes. We employed this method to link the peak amplitude of the seismic signal with various dynamic parameters. Here is a summary of the postulated effects of these flow properties on the peak amplitude:

$$A_p = f_1\left(g, W, L, h_p, d_s, \langle u_d\rangle_p, \theta\right), \tag{9}$$

where f_1 represents an unknown function. By dimensional analysis, the general functional relationship can be recast in the dimensionless form:

$$\frac{A_p d_s}{\langle u_d\rangle_p^2} = f_2\left(\frac{g d_s}{\langle u_d\rangle_p^2}, \frac{W}{d_s}, \frac{L}{d_s}, \frac{h_p}{d_s}, \theta\right), \tag{10}$$

where f_2 represents a new unknown function. The dimensionless peak amplitude $A_p d_s/\langle u_d\rangle_p^2$ show a strong correlation with the dimensionless flow depth h_p/d_s with a correlation coefficient of 0.81 (Figure 13), leading to the relationship $A_p \propto \langle u_d\rangle_p^2 d_s^{4.16} h_p^{-5.16}$. However, frictional flows deviate from

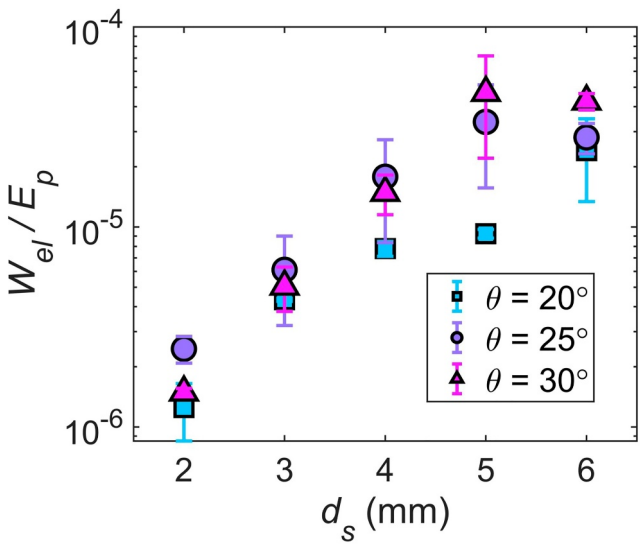

Figure 11. Effects of mean particle diameters d_s and flume inclination angle θ on the ratio of the radiated elastic energy over the potential energy lost W_{el}/E_p.

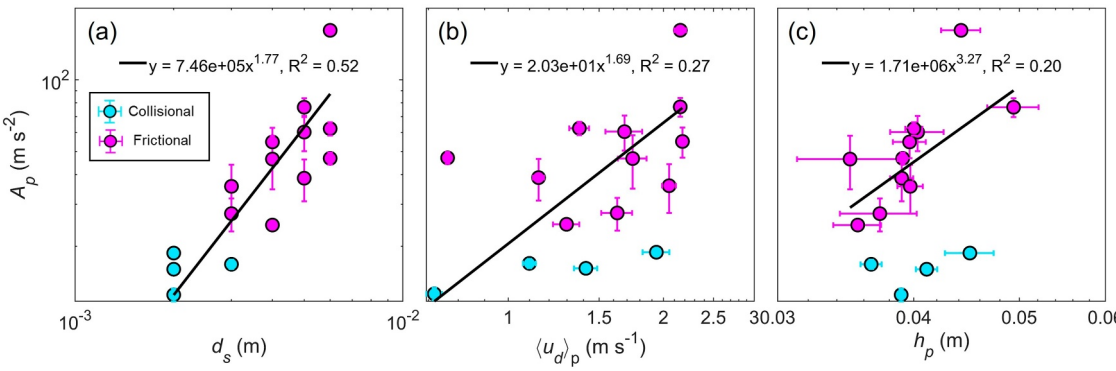

Figure 12. Peak amplitude A_p of seismic signals as a function of flow dynamic parameters under different particle compositions and flume inclinations: (a) mean particle diameters d_s, (b) Peak downslope depth-averaged mean velocity $\langle u_d \rangle_p$, (c) peak flow depth h_p. The indigo and magenta points show cases in the frictional and collisional flow regimes, respectively.

this trend (Figure 13), suggesting that collisional and frictional flow regimes have different relationships between the peak amplitude of seismic signals and flow properties.

4. Discussion

4.1. Effect of Large Particle Proportion on Granular Flow Motion

The effect of large particle proportions on granular flow motion reveals complex dynamics within the system. Experimental results show that as the proportion of large particles increases, the mobility of granular flows initially improves before declining (Figure 7a). This non-linear behavior aligns with the findings of De Haas et al. (2015, 2021), who observed a similar trend in debris flows. They attributed this phenomenon to grain size segregation, where an optimal proportion of gravel enhances flow mobility by facilitating lateral spreading, while excessive gravel content increases frictional resistance, thereby reducing mobility. In our dry granular flow experiments, this transition reflects a comparable mechanism where the interaction between particle sizes is pivotal in determining flow dynamics. This suggests the existence of an optimal particle size composition that maximizes flow mobility.

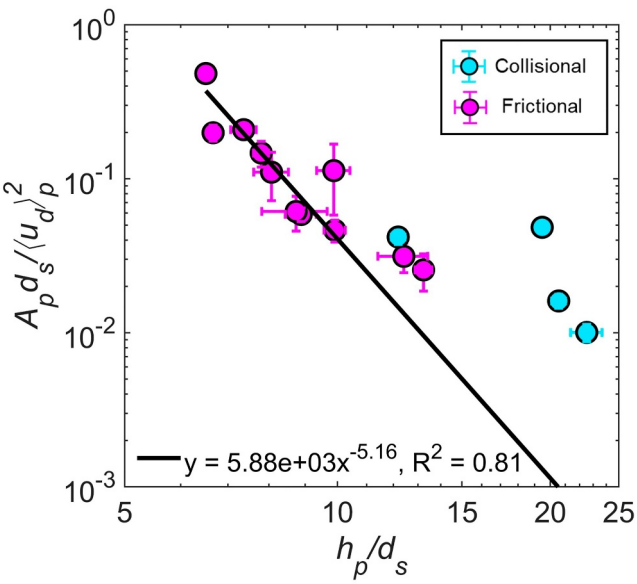

Figure 13. Dimensionless peak amplitude $A_p d_s / \langle u_d \rangle_p^2$ versus dimensionless flow depth h_p/d_s under different particle compositions and flume inclinations. The indigo and magenta points show cases in the frictional and collisional flow regimes, respectively.

To further investigate this behavior, we analyzed the energy transformation characteristics of granular flows. The potential energy loss E_p of the flow is primarily governed by the flume inclination angle, reaching a maximum of 61 J at a 30° slope (Figure 14a). Although variations in mean particle diameter induce minor fluctuations in E_p, E_p consistently increases with flume inclination angle across experiments (Figure 14a). The kinetic energy E_k and the energy conversion efficiency (E_p/E_k) exhibit a consistent pattern of initial increase followed by a decline as the mean particle diameter d_s increases (Figures 14b and 14c). Notably, the maximum E_p/E_k ratio of 0.26 occurs when $d_s = 4$ mm and $\theta = 30°$, suggesting that energy conversion efficiency is tightly linked to particle interactions controlled by the ratio of large to small particles. At lower proportions of large particles, size segregation allows small particles to fill the voids between large particles, facilitating more efficient particle rearrangements, enhanced momentum transfer, and reduced interparticle friction, thereby promoting higher mobility (Jing et al., 2017). However, as the proportion of large particles increases, particle contacts become more constrained, leading to localized jamming, higher frictional resistance, and reduced flow mobility. This interplay between collisional and frictional forces can be interpreted within the rheological framework proposed by Jop et al. (2006), who demonstrated that the transition between frictional and collisional regimes depends on the inertial number, which incorporates both shear rate and particle size as key factors controlling flow

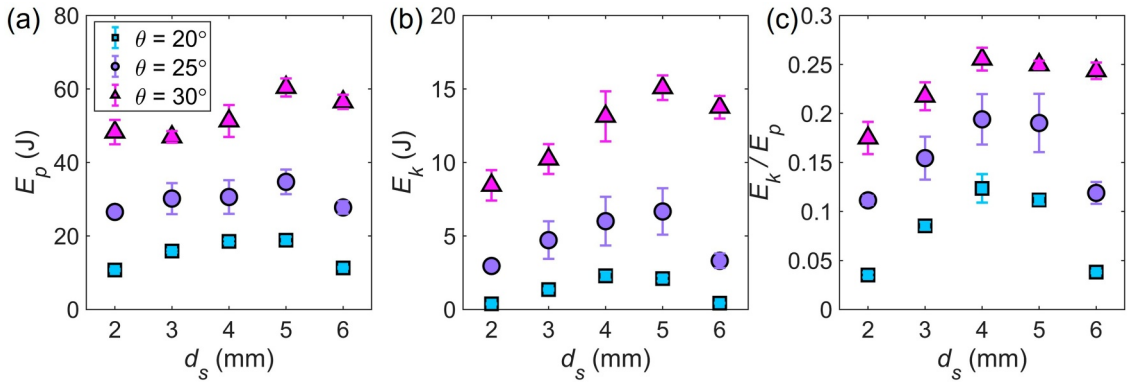

Figure 14. Effects of mean particle diameters d_s and flume inclination angle θ on the (a) potential energy lost E_p, (b) kinetic energy E_k, and (c) ratio of the kinetic energy over the potential energy lost E_p/E_k. Squares, circles and triangles show cases with $\theta = 20°$, 25° and 30°, respectively.

behavior. In our experiments, increasing shear rate (via steeper slopes) and variations in particle size composition jointly modify the packing structure and interparticle contacts, thereby shifting the balance between frictional and collisional stresses in a manner qualitatively consistent with the rheological transitions described by Jop et al. (2006). These findings highlight the importance of gravitational potential-to-kinetic energy conversion and its modulation by particle composition, providing valuable insights into the dynamics of both natural and experimental granular flows. Future studies could explore the role of additional factors, such as particle shape and moisture content, to further refine our understanding of granular flow rheology.

The velocity profiles observed in our flume experiments consistently exhibit an upper plug-like region with nearly uniform velocity across a wide range of slope angles and grain-size combinations (Figures S3 and S4 in Supporting Information S1). However, due to the camera setup and the presence of a basal blind zone approximately 5 mm in height, the lowermost part of the flow—where basal shear is expected to be most intense—remains unobservable. Consequently, only a subset of the flows, primarily those at lower inclinations or with finer grains (i.e., friction-dominated regimes), show visible basal shear layers characterized by strong velocity gradients. In cases involving larger particles, particularly at higher slopes, the plug region appears more pronounced and may extend deeper into the flow. This may reflect not only enhanced collisional behavior but also vertical grain-size segregation effects, as coarser particles tend to accumulate toward the surface due to kinetic sieving. These structural features are broadly consistent with the findings of Kaitna et al. (2007, 2014) and Nagl et al. (2020), who demonstrated that the shape and extent of plug flow in granular-fluid mixtures depend sensitively on both rheology and segregation dynamics. The convexity of the velocity profiles observed at steep slopes and smaller particle sizes further suggests a transition toward collisional flow regimes, in line with the Herschel–Bulkley-type behavior observed in prior drum and flume experiments.

Numerous laboratory experiments have been conducted to understand granular flow dynamics under varying conditions of granulometry and slope (De Haas et al., 2015; Forterre and Pouliquen, 2008; Roelofs et al., 2022; Sakai et al., 2019). These studies have shown that flow behavior transitions from frictional to collisional regimes as the slope increases and the particle interactions become more dynamic. The influence of particle size distribution on flow mobility and shear behavior has also been widely explored (De Haas et al., 2015; Iverson, 1997). Notably, Piantini et al. (2023) examined how solid concentration and grain size influence seismic wave generation, highlighting that finer grains lead to more distributed and lower-energy signals, while coarser grains enhance impulsive characteristics. Our findings expand upon this framework by systematically investigating how particle composition and slope jointly control both flow regimes and seismic responses, thereby bridging the gap between granular rheology and seismogenesis.

4.2. Seismic Signatures Modulated by Flow Regimes and Stress Mechanisms

The influence of flow regimes on seismic signal characteristics is quantitatively demonstrated through the analysis of peak amplitude (A_p) and PSD, revealing a distinct two-segment relationship with the Savage number (N_{sav}) (Figure 15). This transition reflects the fundamental shift in stress transmission and energy dissipation mechanisms as granular flows evolve from frictional to collisional regimes. The deviation of the power-law

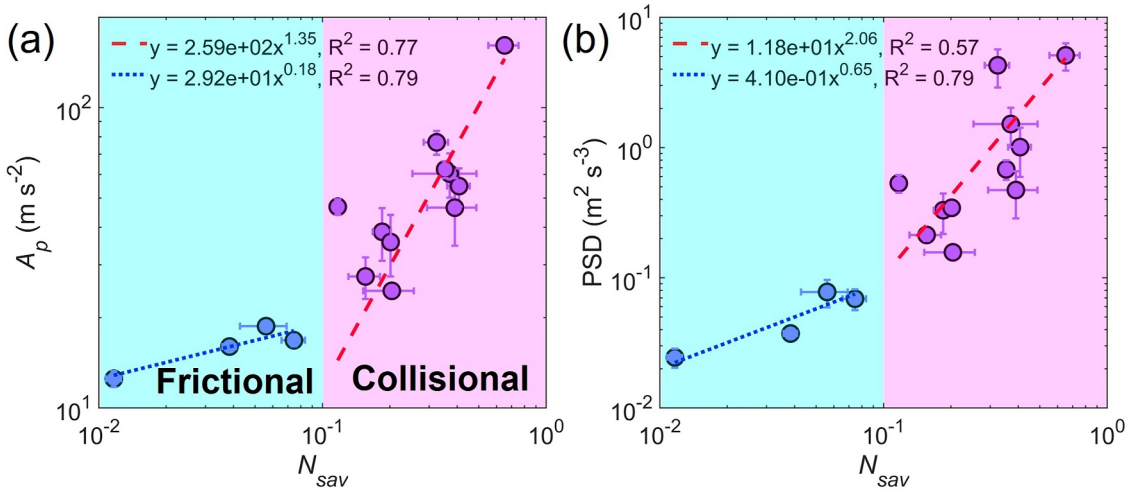

Figure 15. (a) Peak amplitude A_p and (b) peak Power spectral density (PSD) as a function of the savage number. The indigo and magenta points show cases in the frictional and collisional flow regimes, respectively.

relationship between the dimensionless peak amplitude $(A_p d_s/\langle u_d\rangle_p^2)$ and the dimensionless flow depth (h_p/d_s) for frictional flows (Figure 13) indicates that the quasi-static stress mechanisms in this regime exert a considerable influence on seismic signals. This observation supports the framework proposed in previous studies, where stress transmission in frictional flows is dominated by force chains and sustained interparticle contacts, resulting in stable low-amplitude seismic signals (Ancey & Evesque, 2000; Savage and Hutter, 1989; Zhang et al., 2021a).

The two-segment relationship becomes more evident in Figure 15, where both A_p and PSD exhibit a gradual increase with N_{sav} in the frictional regime, followed by a sharp increase in the collisional regime ($N_{sav} > 0.1$). In the frictional regime, energy dissipation is controlled by long-lasting particle contacts and quasi-static deformation, while in the collisional regime, rapid particle rearrangement and binary collisions dominate. These observations are consistent with those of Du et al. (2023), who demonstrated that basal stress metrics transition from being controlled by static contact forces in the frictional regime to being governed by dynamic collisional forces in the collisional regime. The critical value of $N_{sav} \approx 0.1$ marks the threshold at which inertial forces begin to outweigh quasi-static forces, leading to higher stress fluctuations and seismic amplitudes. We adopt the empirical threshold of $N_{sav} = 0.1$ to distinguish between frictional and collisional flows (De Haas et al., 2015; Iverson, 1997; Savage and Hutter, 1989). However, it is important to recognize that collisional and frictional mechanisms often coexist in granular flows, as also emphasized by Ancey and Evesque (2000), who demonstrated that granular shear flows frequently exhibit mixed frictional-collisional regimes depending on solid concentration and shear conditions. In this context, the current classification primarily identifies the dominant mechanism prevailing under specific experimental conditions. Besides, the two-segment power-law relationships observed in Figure 15 are not intended as mechanistic models but serve as empirical fits that highlight the contrasting scaling behaviors in frictional and collisional regimes. The lower slope in the frictional regime reflects limited signal variability under quasi-static stress transmission, while the steeper slope in the collisional regime indicates increased seismic energy release driven by dynamic particle collisions.

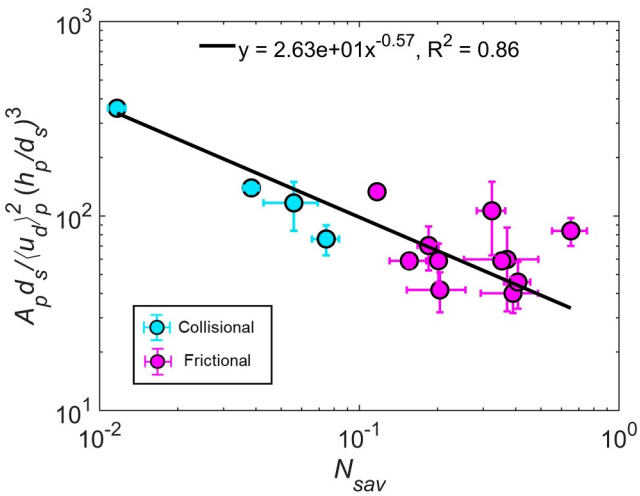

Figure 16. Dimensionless peak amplitude $(A_p d_s/\langle u_d\rangle_p^2)(h_p/d_s)^3$ versus savage number N_{sav}. The indigo and magenta points show cases in the frictional and collisional flow regimes, respectively.

To unify the scaling of seismic signal characteristics across these regimes, we introduce a dimensionless parameter, $(A_p d_s/\langle u_d\rangle_p^2)(h_p/d_s)^3$, which collapses the data into a single power-law relationship with N_{sav} (Figure 16). The scaling exponent of approximately −0.57 reflects the diminishing seismic generation efficiency with increasing inertial effects, indicating that collisional flows with higher Nsav produce relatively less seismic energy per unit of flow energy due to enhanced dissipation and complex multi-particle interactions. This result

underscores the utility of N_{sav} as a unifying descriptor for granular flow regimes, providing insights into the transition mechanisms governing seismic signal variability.

The deviations observed in frictional flows (Figure 13), the two-segment behavior of A_p and PSD with N_{sav} (Figure 15), and the unified dimensionless scaling relationship (Figure 16) collectively support the central hypothesis that seismic signal generation in granular flows reflects the combined influence of flow regime and granular interaction dynamics. Specifically, frictional regimes dominated by sustained interparticle contacts produce stable low-amplitude seismic signals, while collisional regimes exhibit higher seismic amplitudes and variability due to intermittent high-energy particle collisions. These experimental observations demonstrate how granular flow transitions are encoded in seismic signal characteristics, providing a robust framework for interpreting flow regimes from seismic data. Such insights have direct implications for geophysical hazard monitoring, where seismic observations may enable real-time assessments of flow dynamics and regime transitions in natural debris flows and avalanches.

Following the analysis of the Savage number, the underlying stress components governing granular flow can be further interpreted by distinguishing between inertial and quasi-static contributions, as formulated by Iverson (1997). The inertial stress, associated with grain collisions and velocity fluctuations, is estimated as $\sigma_i \sim \rho_s \dot{\gamma}^2 {d_s}^2$, scaling with the square of the shear rate and reflecting the dynamic agitation of the granular mass. In contrast, the quasi-static stress, representing sustained interparticle contacts and Coulomb sliding, is given by $\tau \sim \rho_s g h \tan \phi$, and increases with the submerged weight of the granular layer. The balance between these two stress terms provides a mechanistic explanation for the observed transitions in flow regime, whereby inertial stresses dominate in highly sheared collisional flows, and quasi-static stresses govern dense frictional flows.

The relationships between seismic signal characteristics and stress metrics reveal the dominant influence of collisional stress over frictional stress in granular flows (Figure 17). A distinct two-segment behavior is observed in the correlation between peak amplitude (A_p) and PSD with inertial stress (σ_i). Frictional flows exhibit a weak gradual increase, while collisional flows show a pronounced power-law growth. In contrast, the dependence of A_p and PSD on shear stress (τ) is weaker and less systematic, suggesting that the localized dynamics of particle collisions primarily govern seismic signal variability.

This two-segment relationship with collisional stress reflects the transition between flow regimes. In frictional flows, stress transmission is dominated by long-lasting particle contacts and force chains, leading to low-frequency, low-amplitude seismic signals. Collisional flows, however, are characterized by rapid particle rearrangements and dynamic impacts, resulting in higher seismic amplitudes and frequencies. These findings are consistent with observations by Forterre and Pouliquen (2008), who demonstrated that binary collisions dominate energy dissipation and stress fluctuations in high-shear granular flows, and by Campbell (2002), who highlighted the role of inertial stresses in governing flow behavior in dense granular systems. The relatively weak dependence on shear stress can be attributed to its nature as a bulk-averaged measure of sustained interparticle contact forces, which evolve slowly compared to dynamic collisional processes. In frictional flows, τ primarily reflects quasi-static frictional networks that resist shear deformation, leading to limited variability. Even in collisional flows, where τ increases with shear rate, its contribution to seismic signals remains secondary compared to the rapidly fluctuating collisional stresses (σ_i). Similar stress partitioning behavior has been observed in granular flow studies, where dynamic stresses dominate seismic signal generation in collisional regimes (da Cruz et al., 2005).

The dominance of collisional stress over frictional stress in seismic signal generation underscores the importance of localized particle interactions in granular flows. While shear stress provides a baseline contribution, it is the dynamic, fluctuating nature of collisional stress that drives the variability and intensity of seismic signals. In frictional regimes, collisional stress is constrained by the quasi-static force transmission, limiting its contribution to seismic activity. As collisional stress becomes dominant in high-shear conditions, rapid particle impacts generate stress fluctuations, amplifying seismic signals. This regime-dependent scaling reflects the theoretical prediction (Mitarai and Nakanishi, 2005) that increasing shear rates shift granular flows from quasi-static frictional behavior toward dynamic collisional regimes where stress transmission becomes dominated by rapid particle collisions. Our data provide experimental support for this transition, as seen in the sharp increase in seismic amplitude and inertial stress metrics with the Savage number. These results provide a new mechanistic understanding of how seismic signals reflect flow regime transitions in granular flows, demonstrating that collisional stresses, rather than bulk shear stresses, play the dominant role in seismogenesis. This insight enables

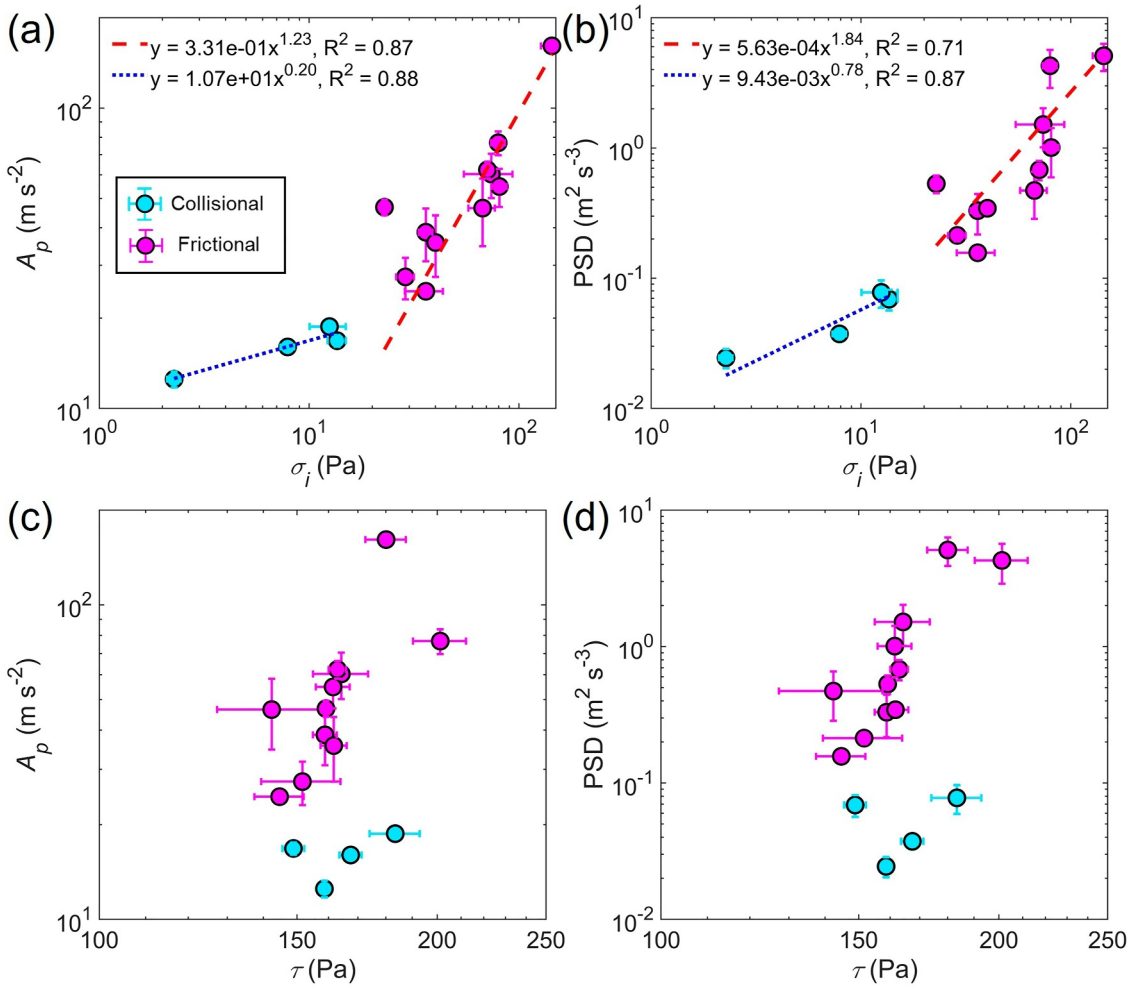

Figure 17. Peak amplitude A_p, and peak Power spectral density (PSD) as a function of (a, b) the inertial stress σ_i and (c, d) the shear stress τ. The indigo and magenta points show cases in the frictional and collisional flow regimes, respectively.

more accurate interpretations of seismic signals from natural flows such as debris flows and avalanches, offering a framework to infer flow regimes, mobility states, and energy dissipation processes from seismic records. Moreover, the dimensionless scaling relationships established in this study provide a basis for designing laboratory experiments and interpreting field data in a unified, physically grounded manner.

4.3. Experimental Evaluation of Seismic Signal Models in Different Flow Regimes

Understanding the seismic signals generated by debris flows is essential for advancing early warning systems and improving interpretations of seismic data. Several theoretical models have been proposed to relate granular flow dynamics to high-frequency seismic radiation, particularly in the >1 Hz range. Among them, the model developed by Farin, Tsai, et al. (2019), building upon the framework of Tsai et al. (2012), attributes the signal to the cumulative effect of numerous random particle impacts onto the bed. For simplification, this "thin-flow" model assumes particles striking the substrate vertically and individually, following the Hertzian contact theory. In contrast, Zhang et al. (2021a) extended this approach by introducing a "force-chain" model in which particle clusters intermittently transmit stress as collective structures, thereby influencing the basal impulse and resulting seismic signal.

We implemented both the thin-flow model from Farin, Tsai, et al. (2019) and the force-chain model from Zhang et al. (2021a) to estimate the PSD of basal force fluctuations in our experiments. The analytical expressions and model parameters are adapted from the formulations summarized in Arran et al. (2021) and Li et al. (2025), which provide a systematic derivation of impulse-based models for high-frequency ground motion.

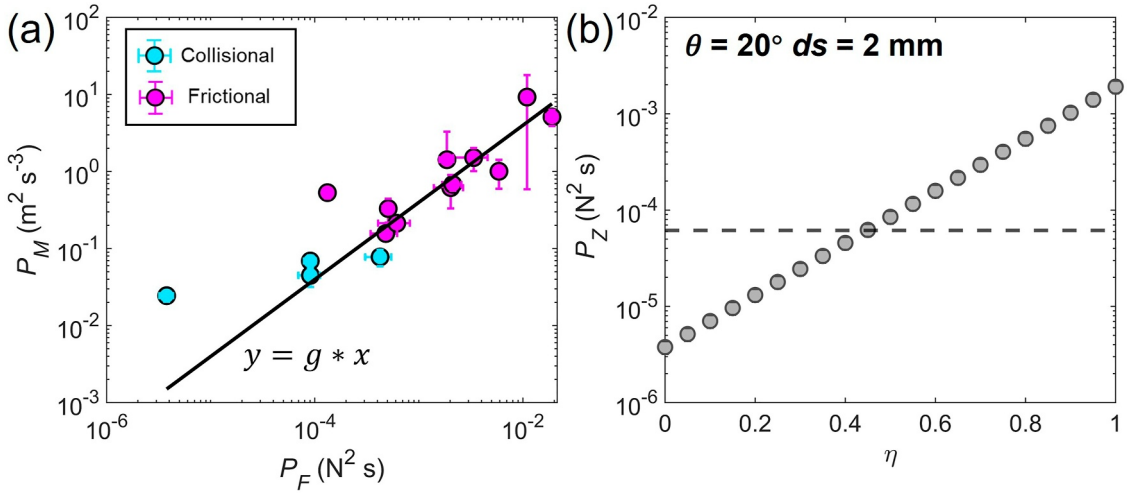

Figure 18. (a) Comparison between measured seismic signal power spectra (P_M) and model predictions (P_F) from the thin-flow model (Farin, Tsai, et al., 2019) across different flow regimes. The black solid line represents a best-fit of the form $y = g * x$. (b) Theoretical basal force power spectra (P_z) calculated using the force-chain model (Zhang et al., 2021a) under varying values of η, specifically for the experiment with $\theta = 20°$ and $d_s = 2$ mm. The black dashed line represents the corresponding value P_{z0}, inferred from the thin-flow model fit in panel Error bars indicate standard deviations derived from three repeated experimental trials.

For the thin-flow model, the PSD of basal force fluctuations is given by:

$$P_F = \frac{\pi^2(1+\lambda)^2\rho_s^2 S\phi d^3 v^3 \chi(\nu)^2}{36}, \tag{11}$$

where $\lambda = 0.2$ is the restitution coefficient ratio, $\rho_s = 2550$ kg/m^3 the grain density, $S = 0.08 \times 0.05$ m^2 the basal contact area, ϕ the solid fraction, d the particle diameter, v the flow velocity, and $\chi(\nu)$ is a dimensionless factor dependent on the particle velocity fluctuation ratio $\nu = \delta u/v$, with:

$$\chi(\nu) \approx 0.23\sqrt{1+\frac{\nu^2}{0.18}}. \tag{12}$$

In the force-chain model proposed by Zhang et al. (2021a), the PSD is modified to include the contribution of collective impacts transmitted through force chains, resulting in:

$$P_Z = \frac{\pi^2(1+\lambda)^2\rho_s^2 S\phi d^{3-2\eta} v^3 h^{2\eta}\chi(\nu)^2}{\left[36\left(\cos\left(\frac{\pi}{6}\right)\right)^{2\eta}\right]}. \tag{13}$$

Here, h is flow depth and $\eta \in [0,1]$ characterizes the fraction of basal impulse transmitted through force chains, ranging from purely individual impacts ($\eta = 0$) to fully force-chain-dominated behavior ($\eta = 1$). At $\eta = 0$, the force-chain formulation collapses to the thin-flow model.

Because of the lack of precise constraints on parameters governing seismic wave propagation—such as source–receiver distance, attenuation, and near-surface structure—we do not explicitly model path effects. Instead, our goal is to assess whether each model captures the essential scaling behavior of signal generation mechanisms under different flow regimes. Therefore, we directly compare the PSDs of basal force fluctuations predicted by the models with the observed PSDs of seismic signals to jointly analyze their consistency in both frequency content and regime dependence. This approach focuses on identifying the dominant physical processes rather than reproducing absolute ground motion amplitudes.

Figure 18a compares the model-predicted basal force power spectrum P_F, based on the thin-flow model of Farin, Tsai, et al. (2019), with the experimentally measured power P_M across different flow regimes. The black solid line represents a linear best-fit in the form of $y = g * x$, where most data points align closely with the fit. This

alignment indicates that, under a wide range of conditions, the thin-flow model reliably captures the magnitude of basal force fluctuations. Notably, this validation also applies when interpreting Zhang et al. (2021a)'s force-chain model with $\eta = 0$, which mathematically reduces to the Farin formulation.

However, one data point deviates significantly from the fitted trend. This outlier corresponds to a low-energy frictional flow with a slope of $\theta = 20°$ and small particle size $d_s = 2$ mm. Under this condition, the flow is dense, slowly shearing, and likely dominated by frictional rather than collisional interactions. Mapping the vertical deviation of this point onto the fitted regression allows us to estimate the model-predicted signal for $\eta = 0$, denoted as P_{z0}. We then use Zhang et al. (2021a)'s force-chain model to back-calculate the corresponding value of η, yielding an estimate of $\eta = 0.45$ (Figure 18b). This suggests that nearly half of the basal force fluctuations under this condition may be attributed to collective force-chain interactions rather than isolated particle impacts. Among the four frictional-flow cases in our data set, only this particular run (20°, 2 mm) exhibits such a large deviation. A plausible explanation lies in the Savage number N_{Sav} associated with each run. The deviating case corresponds to a low $N_{\mathrm{Sav}} \approx 0.01$, indicating strong dominance of quasi-static stress. In contrast, the remaining three frictional-flow cases exhibit moderate values of $N_{\mathrm{Sav}} \approx 0.04 - 0.08$, implying relatively more dynamic interactions and weaker force-chain cohesion.

Frictional regimes are typically characterized by dense packing, enduring interparticle contacts, and reduced agitation, all of which enhance the formation of load-bearing structures such as force chains (Forterre and Pouliquen, 2008; Furbish et al., 2008). Such chains play a dominant role in transmitting stress in slow friction-dominated flows, whereas their influence is diminished in highly agitated collisional regimes.

Accordingly, our findings indicate that while the thin-flow model performs well across most regimes, it tends to underestimate signal strength under strongly frictional conditions. Force-chain model, which incorporates both particle-scale impacts and collective chain effects via the parameter η, provides a more general framework for interpreting basal force signals. As shown in Figure 18b, the predicted P_z increases with η, suggesting that neglecting force-chain effects can lead to substantial underestimation of seismic energy in dense flows. This highlights the importance of incorporating stress transmission heterogeneity in debris-flow seismic modeling, particularly in flows governed by frictional rheology.

4.4. Implications and Limitations

In this study, we adopted a binary mixture of glass beads to control particle composition while simplifying the experimental design. Although this setup does not capture the full complexity of natural debris flows, which often contain a broad and continuous spectrum of particle sizes (Iverson, 1997), it offers significant advantages in isolating the effects of particle size interactions on flow dynamics and seismic responses. The use of two distinct sizes enables controlled exploration of collisional regimes, stress distribution, and kinetic transitions, which may otherwise be obscured in polydisperse mixtures. Similar binary or simplified size distributions have been used in previous experimental studies (Bagnold, 1954; Chik & Vallejo, 2005; Forterre and Pouliquen, 2008; Tripathi and Khakhar, 2011) to identify fundamental mechanisms in granular flow behavior. Recent studies have further explored the impact of particle size distribution on flow dynamics and seismic signal generation. For instance, Bachelet et al. (2023) investigated acoustic emissions from nearly steady granular flows, highlighting the role of particle interactions in seismic wave generation. Zrelak et al. (2024) examined basal force fluctuations in granular flows, linking macroscopic flow descriptions to bed forces and emphasizing the influence of particle size on monitoring signals. These findings underscore the relevance of simplified particle size distributions in understanding granular flow behaviors. Nevertheless, we acknowledge that translating the findings to natural systems requires caution. In real debris flows, broader particle size distributions may lead to enhanced segregation, complex layering effects, and nontrivial flow-front behaviors. Future work should extend this framework by incorporating continuous particle size spectra or field-sampled materials to evaluate how well the proposed dimensionless correlations hold under more realistic conditions.

The use of the mean particle diameter as an input parameter in dimensionless analysis (e.g., Savage number calculation) is a simplification commonly adopted in granular flow studies with binary mixtures (Rognon et al., 2007; Tripathi and Khakhar, 2011). This approach allows for consistent comparison across varying compositions while retaining sensitivity to the overall size scale of the granular assembly. Nevertheless, we acknowledge that some effects related to size polydispersity and bi-disperse interactions may not be fully captured by the mean size alone. This limitation becomes particularly relevant in flows where particles undergo

strong segregation (Jing et al., 2017; Zhou et al., 2020), or where larger particles dominate force transmission and collisional dynamics despite comprising a minority fraction by number (Farin, Tsai, et al., 2019). In such cases, the mean diameter may underestimate the contribution of coarse grains to stress generation and momentum exchange. Therefore, both the mass fraction of large particles and the mean diameter are reported in this study to preserve composition information and ensure comparability with previous studies.

Although the downslope velocity serves as a useful proxy for evaluating dynamic interactions between particles and the ground, the actual impact angle at which particles strike the basal surface plays a significant role in the generation of seismic signals, as highlighted in theoretical and numerical studies (Farin, Tsai, et al., 2019; Tsai et al., 2012). In our current setup, the resolution of PIV-based flow field reconstruction is insufficient to resolve individual particle orientations or impact angles. Consequently, we do not directly quantify this angle, and our analysis assumes that the dominant contribution arises from the downslope component of motion. This is consistent with prior experimental practice (Li et al., 2025; Piantini et al., 2023) and with Farin, Tsai, et al. (2019)'s assumption that particle fluctuation velocity scales with downslope velocity. Nevertheless, we acknowledge that measuring the impact angle would provide a more complete understanding of energy partitioning and stress orientation during collision events. Future work incorporating 3D imaging or particle tracking methods may enable direct observation of particle-ground impact angles and further improve physical modeling of seismic signal generation in granular flows.

It is worth noting that some narrowband features observed in the spectrograms (Figure 8) may be influenced by instrumental resonances of the acceleration sensor rather than purely resulting from particle collisions or propagation effects. This observation is supported by previous studies showing that even well-isolated sensors can exhibit system-induced frequency peaks in controlled granular flow experiments (Bachelet et al., 2023). Given that the typical contact frequencies between particles—calculated from Hertzian contact theory—fall far beyond the measurable range of our sensors (tens to hundreds of kHz), the low-frequency content observed here is more reflective of the collective dynamics and energy fluctuations of the flow rather than individual particle collisions. Theoretical predictions based on Hertzian contact models suggest that interparticle collisions among 2–6 mm glass beads generate signals with mean frequencies ranging from approximately 51 to 219 kHz (Bachelet et al., 2023), far exceeding the measurable range in our experimental setup. Due to our sampling frequency limit of 25.6 kHz, signal analysis is constrained to the 0–10 kHz range, which captures low-frequency energy modulations (<10 kHz) rather than the high-frequency content associated with individual particle contacts. As such, we focus on the amplitude and power-related characteristics of the seismic signals rather than the frequency-based scaling.

5. Conclusions

We design flume experiments to simulate the flow of granular materials with varying compositions under dam-break conditions, focusing on the effects of particle composition on flow dynamics and seismic signals to understand the relationship between flow regimes, dynamic parameters, and seismic responses. The following conclusions were drawn:

1. Flow mobility exhibits a non-monotonic dependence on particle size, with an optimal proportion of large particles maximizing the mean velocity. Increasing flume inclination further increases mean flow velocity and reduces flow duration, indicating enhanced inertial effects.
2. Seismic signal amplitudes, power spectral densities, and radiated energies increase with both particle size and flume inclination, reflecting the strong coupling between granular flow dynamics and seismic energy generation.
3. Seismic signals of frictional and collisional flows exhibit a two-segment positive correlation with the Savage number and collisional stress. This reflects the dominant role of particle collisions in seismic signal generation and highlights the influence of flow regimes on collision dynamics and their seismic signatures.

This study aims to advance the understanding of granular flow mechanisms and seismic signatures, offering a foundation for geophysical hazard monitoring and experimental studies. Future work should refine stress characterization by improving the measurement and modeling of both frictional (shear) and collisional stress components, and further explore their coexistence to develop more comprehensive models of granular flow behavior.

Conflict of Interest

The authors declare no conflicts of interest relevant to this study.

Data Availability Statement

The experimental data supporting this research are available online at https://figshare.com/s/21158ec2096e-f95aafff (Zhou et al., 2025c). The codes used in this study are available online at https://figshare.com/s/bc2710ba723c29f88595 (Zhou et al., 2025b).

Acknowledgments
The authors thank Editor Joel Sankey, Associate Editor, and two anonymous reviewers for their thoughtful comments and suggestions, which helped improve the article. This work was financially supported by the National Natural Science Foundation of China (Grant 42425702, 424120104002, and 42474077).

References

Allstadt, K. E., Farin, M., Iverson, R. M., Obryk, M. K., Kean, J. W., Tsai, V. C., et al. (2020). Measuring basal force fluctuations of debris flows using seismic recordings and empirical green's functions. *Journal of Geophysical Research-Earth Surface*, *125*(9), e2020JF005590. https://doi.org/10.1029/2020jf005590

Ancey, C., & Evesque, P. (2000). Frictional-collisional regime for granular suspension flows Down an inclined channel. *Physical Review E*, *62*(6), 8349–8360. https://doi.org/10.1103/physreve.62.8349

Arattano, M., & Marchi, L. (2005). Measurements of debris flow velocity through cross-correlation of instrumentation data. *Natural Hazards & Earth System Sciences & Discussions*, *5*(1), 137–142. https://doi.org/10.5194/nhess-5-137-2005

Arran, M. I., Mangeney, A., De Rosny, J., Farin, M., Toussaint, R., & Roche, O. (2021). Laboratory landquakes: Insights from experiments into the high-frequency seismic signal generated by geophysical granular flows. *Journal of Geophysical Research-Earth Surface*, *126*(5), e2021JF006172. https://doi.org/10.1029/2021jf006172

Bachelet, V., Mangeney, A., Toussaint, R., de Rosny, J., Arran, M. I., Farin, M., & Hibert, C. (2023). Acoustic emissions of nearly steady and uniform granular flows: A proxy for flow dynamics and velocity fluctuations. *Journal of Geophysical Research: Earth Surface*, *128*(4), e2022JF006990. https://doi.org/10.1029/2022jf006990

Bagnold, R. A. (1954). Experiments on a gravity-free dispersion of large solid spheres in a newtonian fluid under shear. *Proceedings of the Royal Society of London Series a-Mathematical and Physical Sciences*, *225*, 49–63.

Bardou, E., Bonnard, C., & Vulliet, L. (2003). *Methodology of debris flows diagnosis on an alpine watershed* (pp. 23–27). International Conference on Fast Slope Movements.

Boore, D. M., & Thompson, E. M. (2014). Path durations for use in the stochastic-method simulation of ground motions. *Bulletin of the Seismological Society of America*, *104*(5), 2541–2552. https://doi.org/10.1785/0120140058

Burtin, A., Bollinger, L., Vergne, J., Cattin, R., & Nábělek, J. (2008). Spectral analysis of seismic noise induced by Rivers: A new tool to monitor spatiotemporal changes in stream hydrodynamics. *Journal of Geophysical Research*, *113*(B5), B05301. https://doi.org/10.1029/2007jb005034

Campbell, C. S. (2002). Granular shear flows at the elastic limit. *Journal of Fluid Mechanics*, *465*, 261–291. https://doi.org/10.1017/s002211200200109x

Chalk, C. M., Peakall, J., Keevil, G., & Fuentes, R. (2021). Spatial and temporal evolution of an experimental debris flow, exhibiting coupled fluid and particulate phases. *Acta Geotechnica*, *17*(3), 965–979. https://doi.org/10.1007/s11440-021-01265-y

Chik, Z., & Vallejo, L. E. (2005). Characterization of the angle of repose of binary granular materials. *Canadian Geotechnical Journal*, *42*(2), 683–692. https://doi.org/10.1139/t04-118

Chmiel, M., Walter, F., Wenner, M., Zhang, Z., McArdell, B. W., & Hibert, C. (2021). Machine learning improves debris flow warning. *Geophysical Research Letters*, *48*(3), e2020GL090874. https://doi.org/10.1029/2020gl090874

Choi, C. E., & Song, P. (2023). New unsaturated erosion model for landslide: Effects of flow particle size and debunking the importance of frictional stress. *Engineering Geology*, *315*, 107024. https://doi.org/10.1016/j.enggeo.2023.107024

Cook, K. L., & Dietze, M. (2022). Seismic advances in process geomorphology. *Annual Review of Earth and Planetary Sciences*, *50*(1), 183–204. https://doi.org/10.1146/annurev-earth-032320-085133

Cui, P., Zeng, C., & Lei, Y. (2015). Experimental analysis on the impact force of viscous debris flow. *Earth Surface Processes and Landforms*, *40*(12), 1644–1655. https://doi.org/10.1002/esp.3744

Cui, Y., Fang, J., Li, Y., & Liu, H. (2022). Assessing effectiveness of a dual-barrier system for mitigating granular flow hazards through DEM-DNN framework. *Engineering Geology*, *306*, 106742. https://doi.org/10.1016/j.enggeo.2022.106742

Cui, Y., Li, Y., Tang, H., Turowski, J. M., Yan, Y., Bazai, N. A., et al. (2024). A digital-twin platform for cryospheric disaster warning. *National Science Review*, *11*(10). https://doi.org/10.1093/nsr/nwae300

da Cruz, F., Emam, S., Prochnow, M., Roux, J. N., & Chevoir, F. (2005). Rheophysics of dense granular materials: Discrete simulation of plane shear flows. *Physical Review E - Statistical, Nonlinear and Soft Matter Physics*, *72*(2), 021309. https://doi.org/10.1103/physreve.72.021309

De Haas, T., Aberg, A. S., Walter, F., & Zhang, Z. (2021). Deciphering seismic and normal-force fluctuation signatures of debris flows: An experimental assessment of effects of flow composition and dynamics. *Earth Surface Processes and Landforms*, *46*(11), 2195–2210. https://doi.org/10.1002/esp.5168

De Haas, T., Braat, L., Leuven, J. R. F. W., Lokhorst, I. R., & Kleinhans, M. G. (2015). Effects of debris flow composition on runout, depositional mechanisms, and deposit morphology in laboratory experiments. *Journal of Geophysical Research: Earth Surface*, *120*(9), 1949–1972. https://doi.org/10.1002/2015jf003525

Du, J., Zhou, G. G. D., & Cui, K. F. E. (2023). Microscopic description of basal stress generated by granular free-surface flows. *Journal of Geophysical Research: Earth Surface*, *128*(5), e2022JF006953. https://doi.org/10.1029/2022jf006953

Duan, Y., Jing, L., Umbanhowar, P. B., Ottino, J. M., & Lueptow, R. M. (2022). Segregation forces in dense granular flows: Closing the gap between single intruders and mixtures. *Journal of Fluid Mechanics*, *935*, R1. https://doi.org/10.1017/jfm.2022.12

Farin, M., Mangeney, A., de Rosny, J., Toussaint, R., & Trinh, P. T. (2018). Link between the dynamics of granular flows and the generated seismic signal: Insights from laboratory experiments. *Journal of Geophysical Research-Earth Surface*, *123*(6), 1407–1429. https://doi.org/10.1029/2017jf004296

Farin, M., Mangeney, A., de Rosny, J., Toussaint, R., & Trinh, P. T. (2019). Relations between the characteristics of granular column collapses and resultant high-frequency seismic signals. *Journal of Geophysical Research-Earth Surface*, *124*(12), 2987–3021. https://doi.org/10.1029/2019jf005258

Farin, M., Mangeney, A., Rosny, J. d., Toussaint, R., Sainte-Marie, J., & Shapiro, N. M. (2016). Experimental validation of theoretical methods to estimate the energy radiated by elastic waves during an impact. *Journal of Sound and Vibration*, *362*, 176–202. https://doi.org/10.1016/j.jsv.2015.10.003

Farin, M., Tsai, V. C., Lamb, M. P., & Allstadt, K. E. (2019). A physical model of the high-frequency seismic signal generated by debris flows. *Earth Surface Processes and Landforms*, *44*(13), 2529–2543. https://doi.org/10.1002/esp.4677

Forterre, Y., & Pouliquen, O. (2008). Flows of dense granular media. *Annual Review of Fluid Mechanics*, *40*, 1–24. https://doi.org/10.1146/annurev.fluid.40.111406.102142

Furbish, D. J., Schmeeckle, M. W., & Roering, J. J. (2008). Thermal and force-chain effects in an experimental, sloping granular shear flow. *Earth Surface Processes and Landforms*, *33*(13), 2108–2117. https://doi.org/10.1002/esp.1655

Hübl, J., Suda, J., Proske, D., Kaitna, R., & Scheidl, C. (2009). Debris flow impact estimation. In *Proceedings of the 11th international symposium on water management and hydraulic engineering* (pp. 1–5). University od Ss Cyril and Methodius, Faculty of Civil Engineering.

Iverson, R. M. (1997). The physics of debris flows. *Reviews of Geophysics*, *35*(3), 245–296. https://doi.org/10.1029/97rg00426

Iverson, R. M. (2015). Scaling and design of landslide and debris-flow experiments. *Geomorphology*, *244*, 9–20. https://doi.org/10.1016/j.geomorph.2015.02.033

Iverson, R. M., & Denlinger, R. P. (2001). Flow of variably fluidized granular masses across three-dimensional terrain: I. Coulomb mixture theory. *Journal of Geophysical Research*, *106*(B1), 537–552. https://doi.org/10.1029/2000jb900329

Jaeger, H. M., & Nagel, S. R. (1992). Physics of the granular state. *Science*, *255*(5051), 1523–1531. https://doi.org/10.1126/science.255.5051.1523

Jing, L., Kwok, C. Y., & Leung, Y. F. (2017). Micromechanical origin of particle size segregation. *Physical Review Letters*, *118*(11), 118001. https://doi.org/10.1103/physrevlett.118.118001

Jop, P., Forterre, Y., & Pouliquen, O. (2006). A constitutive law for dense granular flows. *Nature*, *441*(7094), 727–730. https://doi.org/10.1038/nature04801

Kaitna, R., Dietrich, W. E., & Hsu, L. (2014). Surface slopes, velocity profiles and fluid pressure in coarse-grained debris flows saturated with water and mud. *Journal of Fluid Mechanics*, *741*, 377–403. https://doi.org/10.1017/jfm.2013.675

Kaitna, R., Rickenmann, D., & Schatzmann, M. (2007). Experimental study on rheologic behaviour of debris flow material. *Acta Geotechnica*, *2*, 71–85. https://doi.org/10.1007/s11440-007-0026-z

Kokelaar, B. P., Graham, R. L., Gray, J. M. N. T., & Vallance, J. W. (2014). Fine-grained linings of leveed channels facilitate runout of granular flows. *Earth and Planetary Science Letters*, *385*, 172–180. https://doi.org/10.1016/j.epsl.2013.10.043

Lai, V. H., Tsai, V. C., Lamb, M. P., Ulizio, T. P., & Beer, A. R. (2018). The seismic signature of debris flows: Flow mechanics and early warning at montecito, California. *Geophysical Research Letters*, *45*(11), 5528–5535. https://doi.org/10.1029/2018gl077683

Lavigne, F., Thouret, J. C., Voight, B., Young, K., LaHusen, R., Marso, J., et al. (2000). Instrumental lahar monitoring at merapi Volcano, Central java, Indonesia. *Journal of Volcanology and Geothermal Research*, *100*(1–4), 457–478. https://doi.org/10.1016/s0377-0273(00)00151-7

Li, W., Wang, D., Doi, I., Wang, G., Zhang, Z., Yan, S., & He, S. (2025). Evolution of basal force fluctuations and seismic signals of granular flows and their proxy: Insights from laboratory flume experiments. *Journal of Geophysical Research: Earth Surface*, *130*(1), e2024JF007980. https://doi.org/10.1029/2024jf007980

Lin, Q., Wang, Y., Cheng, Q., Deng, K., Liu, S., & Li, K. (2022). Characteristics of the seismic signal generated by fragmental rockfalls: Insight from laboratory experiments. *Journal of Geophysical Research: Solid Earth*, *127*(11), e2022JB025096. https://doi.org/10.1029/2022jb025096

Major, J. J., & Iverson, R. M. (1999). Debris-flow deposition: Effects of pore-fluid pressure and friction concentrated at flow margins. *GSA Bulletin*, *111*(10), 1424–1434. https://doi.org/10.1130/0016-7606(1999)111<1424:dfdeop>2.3.co;2

Mcardell, B. W., Bartelt, P., & Kowalski, J. (2006). Field observations of basal forces and fluid pore pressure in a debris flow. *Geophysical Research Letters*, *340*, L07406. https://doi.org/10.1029/2006GL029183

McCoy, S. W., Tucker, G. E., Kean, J. W., & Coe, J. A. (2013). Field measurement of basal forces generated by erosive debris flows. *Journal of Geophysical Research-Earth Surface*, *118*(2), 589–602. https://doi.org/10.1002/jgrf.20041

Mitarai, N., & Nakanishi, H. (2005). Bagnold scaling, density Plateau, and kinetic theory analysis of dense granular flow. *Physical Review Letters*, *94*(12), 128001. https://doi.org/10.1103/physrevlett.94.128001

Nagl, G., Hübl, J., & Kaitna, R. (2020). Velocity profiles and basal stresses in natural debris flows. *Earth Surface Processes and Landforms*, *45*(8), 1764–1776. https://doi.org/10.1002/esp.4844

Piantini, M., Gimbert, F., Korkolis, E., Rousseau, R., Bellot, H., & Recking, A. (2023). Solid concentration as a main proxy for basal force fluctuations generated by highly concentrated sediment flows. *Geophysical Research Letters*, *50*(1), e2022GL100345. https://doi.org/10.1029/2022gl100345

Pierson, T. C. (1981). Dominant particle support mechanisms in debris flows at Mt Thomas, New Zealand, and implications for flow mobility. *Sedimentology*, *28*(1), 49–60. https://doi.org/10.1111/j.1365-3091.1981.tb01662.x

Roelofs, L., Colucci, P., & Haas, T. (2022). How debris-flow composition affects bed erosion quantity and mechanisms: An experimental assessment. *Earth Surface Processes and Landforms*, *47*(8), 2151–2169. https://doi.org/10.1002/esp.5369

Rognon, P. G., Roux, J.-N., Naaïm, M., & Chevoir, F. (2007). Dense flows of bidisperse assemblies of disks Down an inclined plane. *Physics of Fluids*, *19*(5), 058101. https://doi.org/10.1063/1.2722242

Sakai, Y., Hotta, N., Kaneko, T., & Iwata, T. (2019). Effects of grain-size composition on flow resistance of debris flows: Behavior of fine sediment. *Journal of Hydraulic Engineering*, *145*(5), 06019004. https://doi.org/10.1061/(asce)hy.1943-7900.0001586

Saló, L., Corominas, J., Lantada, N., Matas, G., Prades, A., & Ruiz-Carulla, R. (2018). Seismic energy analysis as generated by impact and fragmentation of single-block experimental rockfalls. *Journal of Geophysical Research: Earth Surface*, *123*(6), 1450–1478. https://doi.org/10.1029/2017jf004374

Savage, S. B., & Hutter, K. (1989). The motion of a finite mass of granular material down a rough incline. *Journal of Fluid Mechanics*, *199*, 177–215. https://doi.org/10.1017/s0022112089000340

Scheidl, C., Chiari, M., Kaitna, R., Müllegger, M., Krawtschuk, A., Zimmermann, T., & Proske, D. (2013). Analysing debris-flow impact models, based on a small scale modelling approach. *Surveys in Geophysics*, *34*(1), 121–140. https://doi.org/10.1007/s10712-012-9199-6

Song, P. J., & Choi, C. E. (2021). Revealing the importance of capillary and collisional stresses on soil bed erosion induced by debris flows. *Journal of Geophysical Research-Earth Surface*, *126*(5), e2020JF005930. https://doi.org/10.1029/2020jf005930

Stock, J. D., & Dietrich, W. E. (2006). Erosion of steepland valleys by debris flows. *Geological Society of America Bulletin*, *118*(9–10), 1125–1148. https://doi.org/10.1130/b25902.1

Takahashi, T. (2007). *Debris flow: Mechanics, prediction and countermeasures*. Taylor and Francis.

Takahashi, T. (2014). Debris flow (2nd ed., pp. 541–551). https://doi.org/10.1201/b16647

Takahashi, T., Nakagawa, H., Harada, T., & Yamashiki, Y. (1992). Routing debris flows with particle segregation. *Journal of Hydraulic Engineering*, *118*(11), 1490–1507. https://doi.org/10.1061/(asce)0733-9429(1992)118:11(1490)

Thielicke, W., & Stamhuis, E. J. (2014). PIVlab – Towards user-friendly, affordable and accurate digital particle image velocimetry in MATLAB. *Journal of Open Research Software*, *2*. https://doi.org/10.5334/jors.bl

Tripathi, A., & Khakhar, D. V. (2011). Rheology of binary granular mixtures in the dense flow regime. *Physics of Fluids*, *23*(11), 113302. https://doi.org/10.1063/1.3653276

Tsai, V. C., Minchew, B., Lamb, M. P., & Ampuero, J. P. (2012). A physical model for seismic noise generation from sediment transport in rivers. *Geophysical Research Letters*, *39*(2), L02404. https://doi.org/10.1029/2011gl050255

White, D., Take, W., & Bolton, M. (2003). Soil deformation measurement using particle image velocimetry (PIV) and photogrammetry. *Géotechnique*, *53*(7), 619–631. https://doi.org/10.1680/geot.53.7.619.37383

Wiederseiner, S., Andreini, N., Épely-Chauvin, G., Moser, G., Monnereau, M., Gray, J. M. N. T., & Ancey, C. (2011). Experimental investigation into segregating granular flows down chutes. *Physics of Fluids*, *23*(1), 013301. https://doi.org/10.1063/1.3536658

Willert, C. E., & Gharib, M. (1991). Digital particle image velocimetry. *Experiments in Fluids*, *10*(4), 181–193. https://doi.org/10.1007/bf00190388

Yan, Y., Tang, H., Hu, K., Turowski, J. M., & Wei, F. (2023). Deriving debris-flow dynamics from real-time impact-force measurements. *Journal of Geophysical Research: Earth Surface*, *128*(3), e2022JF006715. https://doi.org/10.1029/2022jf006715

Yohannes, B., & Hill, K. M. (2010). Rheology of dense granular mixtures: Particle-size distributions, boundary conditions, and collisional time scales. *Physical Review E*, *82*(6), 061301. https://doi.org/10.1103/physreve.82.061301

Yu, X., Chen, X., Li, W., & Zhang, G. (2021). Spatio-temporal distribution characteristics of debris flow impact pressure and impact velocity on the check dam upstream surface. *Geotechnical & Geological Engineering*, *39*(6), 4093–4111. https://doi.org/10.1007/s10706-020-01662-2

Zhang, Z., He, S., Liu, W., Liang, H., Yan, S., Deng, Y., et al. (2019). Source characteristics and dynamics of the October 2018 Baige landslide revealed by broadband seismograms. *Landslides*, *16*(4), 777–785. https://doi.org/10.1007/s10346-019-01145-3

Zhang, Z., Walter, F., McArdell, B. W., de Haas, T., Wenner, M., Chmiel, M., & He, S. (2021a). Analyzing bulk flow characteristics of debris flows using their high frequency seismic signature. *Journal of Geophysical Research: Solid Earth*, *126*(12), e2021JB022755. https://doi.org/10.1029/2021jb022755

Zhang, Z., Walter, F., McArdell, B. W., Wenner, M., Chmiel, M., de Haas, T., & He, S. (2021b). Insights from the particle impact model into the high-frequency seismic signature of debris flows. *Geophysical Research Letters*, *48*(1), e2020GL088994. https://doi.org/10.1029/2020gl088994

Zheng, H., Shi, Z., de Haas, T., Shen, D., Hanley, K. J., & Li, B. (2022). Characteristics of the impact pressure of debris flows. *Journal of Geophysical Research: Earth Surface*, *127*(3), e2021JF006488. https://doi.org/10.1029/2021jf006488

Zhou, G. G. D., Cui, K. F. E., Jing, L., Zhao, T., Song, D., & Huang, Y. (2020). Particle size segregation in granular mass flows with different ambient fluids. *Journal of Geophysical Research: Solid Earth*, *125*(10), e2020JB019536. https://doi.org/10.1029/2020jb019536

Zhou, G. G. D., & Ng, C. W. W. (2010). Dimensional analysis of natural debris flows. *Canadian Geotechnical Journal*, *47*(7), 719–729. https://doi.org/10.1139/t09-134

Zhou, Q., Tang, H., Hibert, C., Chmiel, M., Walter, F., Dietze, M., & Turowski, J. M. (2025a). Enhancing debris flow warning via machine learning feature reduction and model selection. *Journal of Geophysical Research: Earth Surface*, *130*(4), e2024JF008094. https://doi.org/10.1029/2024jf008094

Zhou, Q., Tang, H., Turowski, J. M., Braun, J., Dietze, M., Walter, F., et al. (2024). Benford's law as debris flow detector in seismic signals. *Journal of Geophysical Research: Earth Surface*, *129*(9), e2024JF007691. https://doi.org/10.1029/2024jf007691

Zhou, X., Cui, Y., Zhang, Z., Ye, L., & Fang, J. (2025b). Codes for "Linking Dynamic Parameters and Seismic Signals of Granular Flows in Different Flow Regimes: An Experimental Assessment of Effects of Particle Composition" [Software]. *figshare*. https://figshare.com/articles/dataset/Codes_for_Linking_Dynamic_Parameters_and_Seismic_Signals_of_Granular_Flows_in_Different_Flow_Regimes_An_Experimental_Assessment_of_Effects_of_Particle_Composition_/28342640

Zhou, X., Cui, Y., Zhang, Z., Ye, L., & Fang, J. (2025c). Dataset for "Linking Dynamic Parameters and Seismic Signals of Granular Flows in Different Flow Regimes: An Experimental Assessment of Effects of Particle Composition" [Dataset]. *figshare*(Version 1). https://figshare.com/articles/dataset/Dataset_for_Linking_Dynamic_Parameters_and_Seismic_Signals_of_Granular_Flows_in_Different_Flow_Regimes_An_Experimental_Assessment_of_Effects_of_Particle_Composition_/28342643

Zrelak, P., Breard, E. C. P., & Dufek, J. (2024). Basal force fluctuations and granular rheology: Linking macroscopic descriptions of granular flows to bed forces with implications for monitoring signals. *Journal of Geophysical Research: Earth Surface*, *129*(7), e2024JF007760. https://doi.org/10.1029/2024jf007760